

# Correlations between X-ray properties and Black Hole Mass in AGN: towards a new method to estimate black hole mass from short exposure X-ray observations

Julian A. Mayers,<sup>1</sup> Kathy Romer,<sup>1</sup> Arya Fahari,<sup>2</sup> John P. Stott,<sup>3</sup> Paul Giles,<sup>1</sup> Philip J. Rooney<sup>1</sup>, A. Bermeo-Hernandez,<sup>1</sup> Chris A. Collins,<sup>4</sup> Matt Hilton,<sup>5</sup> Ben Hoyle,<sup>6,7</sup> Andrew R. Liddle,<sup>8</sup> Robert G. Mann,<sup>8</sup> Christopher J. Miller,<sup>2</sup> Robert C. Nichol,<sup>9</sup> Martin Sahlén,<sup>10</sup> C. Vergara-Cervantes,<sup>1</sup> Pedro T. P. Viana<sup>11,12</sup>

<sup>1</sup>*Astronomy Centre, University of Sussex, Falmer, Brighton, BN1 9QH, UK*

<sup>2</sup>*Astronomy Department, University of Michigan, Ann Arbor, MI 48109, USA*

<sup>3</sup>*Department of Physics, Lancaster University, Lancaster LA1 4YB, UK*

<sup>4</sup>*Astrophysics Research Institute, Liverpool John Moores University, IC2, Liverpool Science Park, 146 Brownlow Hill, Liverpool, L3 5RF, UK*

<sup>5</sup>*Astrophysics & Cosmology Research Unit, School of Mathematics, Statistics & Computer Science, University of KwaZulu-Natal, Durban 4041, SA*

<sup>6</sup>*Universitaets-Sternwarte, Fakultät fuer Physik, Ludwig-Maximilians Universitaet Muenchen, Scheinerstr. 1, D-81679 Muenchen, Germany*

<sup>7</sup>*Max Planck Institute fuer Extraterrestrial Physics, Giessenbachstr. 1, D-85748 Garching, Germany*

<sup>8</sup>*Institute for Astronomy, University of Edinburgh, Royal Observatory, Blackford Hill, Edinburgh, EH9 3HJ, UK*

<sup>9</sup>*Institute of Cosmology and Gravitation, University of Portsmouth, Dennis Sciama Building, Portsmouth, PO1 3FX, UK*

<sup>10</sup>*Department of Physics and Astronomy, Uppsala University, SE-751 20 Uppsala, Sweden*

<sup>11</sup>*Instituto de Astrofísica e Ciências do Espaço, Universidade do Porto, CAUP, Rua das Estrelas, 4150-762 Porto, Portugal*

<sup>12</sup>*Departamento de Física e Astronomia, Faculdade de Ciências, Universidade do Porto, Rua do Campo Alegre, 687, 4169-007 Porto, Portugal*

Accepted XXX. Received YYY; in original form ZZZ

## ABSTRACT

Several investigations of the X-ray variability of active galactic nuclei (AGN) using the normalised excess variance ( $\sigma_{\text{NXS}}^2$ ) parameter have shown that variability has a strong anti-correlation with black hole mass ( $M_{\text{BH}}$ ) and X-ray luminosity ( $L_{\text{X}}$ ). In this study we confirm these previous correlations and find no evidence of a redshift evolution. Using observations from XMM-Newton, we determine the  $\sigma_{\text{NXS}}^2$  and  $L_{\text{X}}$  for a sample of 1091 AGN drawn from the XMM-Newton Cluster Survey (XCS) - making this the largest study of X-ray spectral properties of AGNs. We created light-curves in three time-scales; 10 ks, 20 ks and 40 ks and used these to derive scaling relations between  $\sigma_{\text{NXS}}^2$ ,  $L_{\text{X}}$  (2.0-10 keV range) and literature estimates of  $M_{\text{BH}}$  from reverberation mapping. We confirm the anti-correlation between  $M_{\text{BH}}$  and  $\sigma_{\text{NXS}}^2$  and find a positive correlation between  $M_{\text{BH}}$  and  $L_{\text{X}}$ . The use of  $\sigma_{\text{NXS}}^2$  is practical only for pointed observations where the observation time is tens of kiloseconds. For much shorter observations one cannot accurately quantify variability to estimate  $M_{\text{BH}}$ . Here we describe a method to derive  $L_{\text{X}}$  from short duration observations and used these results as an estimate for  $M_{\text{BH}}$ . We find that it is possible to estimate  $L_{\text{X}}$  from observations of just a few hundred seconds and that when correlated with  $M_{\text{BH}}$ , the relation is statistically similar to the relation of  $M_{\text{BH}}-L_{\text{X}}$  derived from a spectroscopic analysis of full XMM observations. This method may be particularly useful to the eROSITA mission, an all-sky survey, which will detect  $>10^6$  AGN.

**Key words:** galaxies: active – galaxies: nuclei – X-rays: galaxies – quasars: super-massive black holes

## 1 INTRODUCTION

The general consensus in Astronomy is that every large galaxy harbours a super-massive black hole (SMBH) with

masses in a range  $10^6$  to  $10^9 M_\odot$ , e.g. (Ferrarese & Ford 2005). About 10 per cent of these are revealed, at any epoch, by an extremely bright active galactic nucleus (AGN), e.g. (Gandhi 2005) with bolometric luminosities ranging from  $10^{42}$  to  $10^{46}$  ergs $^{-1}$ . Studying the mechanisms underlying AGN activity and feedback is essential to improve our understanding of galaxy evolution e.g. (Sijacki et al. 2007). The importance of the SMBH to the host galaxy is demonstrated by the tight correlation between black hole mass ( $M_{\text{BH}}$ ) and stellar velocity dispersion (Gebhardt et al. 2000; Ferrarese & Merritt 2000; Tremaine et al. 2002; Ferrarese 2002). Similar relations hold between  $M_{\text{BH}}$  and the stellar mass of the galaxy bulge (e.g. Magorrian et al. 1998), and between  $M_{\text{BH}}$  and stellar luminosity concentration parameter (Trujillo et al. 2001).

Stellar velocity dispersions allow a direct measurement of  $M_{\text{BH}}$  (Gebhardt et al. 2000; Ghez et al. 2005) in our own Galaxy and of those in the very local ( $z < 0.025$ ) Universe. However, the technique can only be used if there is not an AGN at their core: an AGN would be so bright as to obscure the starlight from the galactic bulge. Where there is an active core, the best alternative to measure  $M_{\text{BH}}$  is to use reverberation mapping (Blandford & McKee 1982). This technique measures the delay between changes in the continuum emission from the hot gas in the accretion disk and the response to these changes in the broad emission lines in the optical, UV and near IR part of the spectrum. This method, only applicable to Type 1 AGN (i.e. those with broad emission lines) is costly in terms of telescope time because it requires time resolved, high signal to noise, spectroscopy. Therefore, to date, only a few dozen successful measurements have been made. The largest combination of  $M_{\text{BH}}$  measurements from reverberation mapping determined comprises of just 63 AGN (Bentz & Katz 2015), which in turn draws on various other surveys including (Peterson et al. 1998), (Grier et al. 2012), and (Kaspi et al. 2000). Recently, new techniques been developed to estimate  $M_{\text{BH}}$  from X-ray (as opposed to optical) reverberation-mapping (e.g. Kara 2018).

Although reverberation mapping is unlikely, at least in the near term, to deliver SMBH masses for large ( $>100$ ) samples of AGN, it can be used to calibrate indirect methods that are less costly in terms of telescope time. For example, it has been used to calibrate a method that is based on the width of broad optical emission lines measured from single-epoch optical or UV spectroscopy (e.g. Vestergaard 2002).

Another indirect method to measure  $M_{\text{BH}}$  is based on X-ray variability. Since the early days of X-ray astronomy it has been known that X-ray emission is by far the most important contributor to the overall luminosity of AGN (Elvis et al. 1978). X-ray emission from AGN is common: they comprise  $\sim 80\%$  of X-ray point source detections at high Galactic latitude (Gandhi 2005). The X-ray emission mechanism at low (“soft”) frequencies is thought to be produced via thermal bremsstrahlung radiation originating in a hot ionised gas close to the central SMBH (e.g. Di Matteo 2001). At higher (“hard”) frequencies, the emission is thought to be a result of inverse-Compton scattering of UV photons by hot electrons, which in turn generates a power-law spectrum (Rees 1984). The hot electrons originate in the accretion disk around the SMBH, which is heated, through friction, to several thousand degrees Kelvin. The disk radiates thermally in the ul-

traviolet and through interaction with the ultra-relativistic electrons from the corona into the higher energies of the X-ray region. The spectral index of the Comptonised radiation is measured to be  $\Gamma \approx 1.7\text{--}2.2$  (e.g. Nandra & Pounds 1994; George et al. 2000; Sambruna et al. 1999).

AGN X-ray emission demonstrates significant variability over periods of hours to days (e.g. McHardy 1988; Pounds & McHardy 1988). Some have even shorter timescales, of the order of minutes, (e.g. Lawrence et al. 1985). The short timescale of the variability implies that the X-ray emitting region is very compact - since variability is governed by light-crossing time - and hence located close to the SMBH. The most accurate method to quantify X-ray variability of an AGN is to look at the power spectral density function (PSD). Analysis from EXOSAT, (e.g. Lawrence & Papadakis 1993), and later RTXE, (e.g. Uttley et al. 2002), showed that the PSD could be modeled by a powerlaw with slopes of  $\Gamma \simeq -2$ , flattening at some ‘break’ frequency. (McHardy et al. 2006) demonstrated the PSD break timescales increase proportionally with  $M_{\text{BH}}$ . This was also confirmed by (Körding et al. 2007) who also showed that  $M_{\text{BH}}$  and break frequency were intimately related.

Detailed PSD analysis of light-curves from SMBH and black hole binaries (BHB) indicated that the emission engine powering both AGN and BHBs are the same, for although the X-ray variability timescales differ between AGN (from a few hundred seconds upwards) and BHBs (to seconds or less), the power spectra are very similar. Hence the variability difference can be accounted for by the difference in the mass of the central object (e.g. Uttley et al. 2002, Markowitz et al. 2003).

Unfortunately, the PSD method necessitates long (typically tens of kiloseconds) X-ray observations of individual AGN. This is because the lowest observable frequency scales as  $t^{-1}$ , where  $t$  is the observation exposure time. Due to the requirement of long X-ray exposures, the application of this method is not suitable to large samples of AGN. For example, when using the entire 2XMMi catalogue (Watson et al. 2009), (González-Martín & Vaughan 2012) cross-matched with all AGN in the 13th edition of the Veron-Cetty & Veron (2010, VC13 henceforth) catalogue (168,940 quasars and AGN) there are only 104 AGN with exposures  $>40$  ks at  $z < 0.4$ , (from 209 observations) for which they could then estimate the PSD (from a potential sample of  $\sim 6000$  AGN without the restrictions on exposure and redshift). This is the largest sample of PSDs of AGN ever analyzed.

An alternative way to define X-ray variability is the Normalised Excess Variance ( $\sigma_{\text{NXS}}^2$ ) (e.g. Nandra et al. 1997). This method is significantly less costly in terms of X-ray telescope time than PSD. It is given by the formula:

$$\sigma_{\text{NXS}}^2 = \frac{1}{\bar{x}^2} \left[ \frac{1}{N-1} \sum_{i=1}^N (x_i - \bar{x})^2 - \frac{1}{N} \sum_{i=1}^N \sigma_i^2 \right], \quad (1)$$

where  $N$  is the number of time bins in the light-curve of the source,  $\bar{x}$  is the mean count rate,  $x_i$  is the count-rate in bin  $i$  and  $\sigma_i^2$  the error in count rate in bin  $i$ . A positive value of  $\sigma_{\text{NXS}}^2$  implies that intrinsic variability of the source dominates the measurement uncertainty (and vice versa). As

shown by (van der Klis 1997), the  $\sigma_{\text{NXS}}^2$  is simply the integral of the PSD over a frequency interval  $\nu_{\text{min}}$  to  $\nu_{\text{max}}$  i.e:

$$\sigma_{\text{NXS}}^2 = \int_{\nu_{\text{min}}}^{\nu_{\text{max}}} P(\nu) d\nu, \quad (2)$$

where  $\nu_{\text{min}} = T^{-1}$ ,  $\nu_{\text{max}} = 2\Delta T^{-1}$ ,  $T$  is the duration of the observation, and  $\Delta T$  is length of light-curve time bin.

The Poisson uncertainty on an individual measurement of  $\sigma_{\text{NXS}}^2$  has been estimated by (Vaughan et al. 2003a) to be

$$\Delta(\sigma_{\text{NXS}}^2) = \sqrt{\left(\sqrt{\frac{2}{N}} \cdot \frac{\sigma_{\text{err}}^2}{\bar{x}^2}\right)^2 + \left(\sqrt{\frac{\sigma_{\text{err}}^2}{N}} \cdot \frac{2\sigma_{\text{NXS}}}{\bar{x}}\right)} \quad (3)$$

where  $\overline{\sigma_{\text{err}}^2}$  is the mean square error.

When comparing different AGN, the  $\sigma_{\text{NXS}}^2$  values need to be  $k$ -corrected and adjusted to account for differences in observing times, see (Kelly et al. 2013). According to (Middei et al. 2016) these two factors can be accounted for by the scaling relation:

$$^* \sigma_{\text{NXS}}^2 = \sigma_{\text{NXS}}^2 \left( \frac{\Delta t^*}{\Delta t_{\text{obs}}} \right)^{2\beta} (1+z)^{2\beta}, \quad (4)$$

where  $z$  is the redshift of the AGN,  $\Delta t^*$  is a fixed time interval,  $\Delta t_{\text{obs}}$  is the time interval over the observation, and  $\beta$  is estimated to be  $0.10 \pm 0.01$  (e.g. Antonucci et al. 2014). The most comprehensive study, prior to the work presented herein, of the relationship between  $\sigma_{\text{NXS}}^2$  and  $M_{\text{BH}}$  drew upon the ‘‘Catalogue of AGN In the XMM Archive’’ (or CAIXA) published in (Bianchi et al. 2009a). This catalogue contains 168 radio-quiet AGN that were observed by XMM-Newton. Of these 168, 32 have  $M_{\text{BH}}$  estimated from reverberation mapping techniques. The remainder have  $M_{\text{BH}}$  estimated from other techniques, e.g. stellar velocity dispersions, emission lines in the Broad Line Region, or optical luminosity. Regardless of the  $M_{\text{BH}}$  estimation techniques, (Ponti et al. 2012) found a significant anti-correlation between  $M_{\text{BH}}$  and  $\sigma_{\text{NXS}}^2$ . This confirmed work by (O’Neill et al. 2005), which was based on ASCA observations of 46 AGN. However, subsequent work, e.g. (Pan et al. 2015) and (Ludlam et al. 2015) – based on the analysis of 11 and 14 low mass,  $M_{\text{BH}} \leq 10^6 M_{\odot}$ , AGN respectively – suggest that there is a flattening of correlation between variability and  $M_{\text{BH}}$  in the low mass regime.

In addition to the anti-correlation between variability and  $M_{\text{BH}}$  mentioned above, there is also evidence for an anti-correlation between variability and X-ray luminosity, e.g. (Lawrence & Papadakis 1993) (Barr & Mushotzky 1986) (Bianchi et al. 2009a) (O’Neill et al. 2005), (Papadakis 2004) (Zhou et al. 2010) (Ponti et al. 2012). This, in turn, suggests that it may be possible to estimate  $M_{\text{BH}}$  from luminosity measurements, e.g. (Papadakis 2004) (O’Neill et al. 2005). This possibility is attractive because luminosities can be measured from much shorter observations than  $\sigma_{\text{NXS}}^2$ .

In the work presented herein, we have re-examined correlations between the X-ray observables  $L_X$  and  $\sigma_{\text{NXS}}^2$ , and their respective correlations with reverberation mapping determined  $M_{\text{BH}}$ . Our goal was to determine the reliability of

$M_{\text{BH}}$  estimates derived from  $L_X$  measurements alone (i.e. in the case where X-ray variability information is not available). We have explored whether this approach to  $M_{\text{BH}}$  estimation can be applied to data gathered by the eROSITA mission (Predehl et al. 2010). eROSITA will measure hundreds of thousands of AGN  $L_X$  values, however, due to the short exposures of the individual observations comprising the all-sky survey, very few – if any – values of  $\sigma_{\text{NXS}}^2$  will be measured.

An overview of the paper is as follows. Section 2 describes how AGN were identified from the XMM Cluster Survey point source catalogue. Section 3 describes methods used to the measure variability ( $\sigma_{\text{NXS}}^2$ ), X-ray luminosity ( $L_X$ ), and spectral index ( $\Gamma$ ) of the AGN. Section 4 presents the measured correlations between X-ray observables and  $M_{\text{BH}}$ . Section ?? looks ahead to the launch of eROSITA and forecasts the potential to derive  $M_{\text{BH}}$  estimates from eROSITA luminosity measurements. Section 5 presents discussions and future directions. We assume the cosmological parameters  $H_0=70 \text{ km s}^{-1} \text{ Mpc}^{-1}$ ,  $\Omega_{\Lambda}=0.73$  and  $\Omega_M = 0.27$  throughout.

## 2 DATA

The XMM Cluster Survey, (XCS) (Romer et al. 2001) provides an ideal opportunity to define a new sample of X-ray detected AGN. XCS is a serendipitous search for galaxy clusters using all publicly available data in the XMM-Newton Science Archive. In addition to collating detections of extended X-ray sources, i.e. cluster candidates, XCS also identifies serendipitous and targeted point-like X-ray sources. The XCS source catalogue grows with the size of the XMM public archive. At the time of writing, it contained over 250,000 point sources. The data reduction and source detection procedures used to generate the XCS source catalogue are described in (Lloyd-Davies et al. 2011, LD11 hereafter). For our study, we limited ourselves only to point-like sources detected by the XCS Automated Pipeline Algorithm (XAPA) with more than 300 (background subtracted) soft-band photons. LD11 showed that, above that threshold, the XCS morphological classification (point-like versus extended) is robust. There are 12,532 such sources in the current version of the XCS point source catalogue. Using TOPCAT<sup>1</sup>, their positions have been compared to those of known AGN in VC13, and the SDSS-DR12Q Quasar Catalog (Kozłowski 2016, 297,301 quasars).

The matching radius was set to a conservative value of 5 arcsec (LD11 find 95 per cent of matches fall within within 6.6 arcsec with a 1 per cent chance of false identification within 10 arcsec). We find 2039 matches to XCS point sources ( $> 300$  counts): 1,689 sources in VC13 and 513 in SDSS DR12Q, with 163 in common<sup>2</sup>. Figure 1 shows the distribution of separation between XCS point sources and AGN positions in both catalogues. The darker bars are where the separation is  $< 5$  arcsec. After removing sources within  $10^\circ$

<sup>1</sup> <http://www.star.bris.ac.uk/mbt/topcat>

<sup>2</sup> Including XCS point sources with fewer than 300 counts, the number of matches increases to 6,505 sources in VC13 and 6,339 in SDSS DR12, with 890 sources in common.

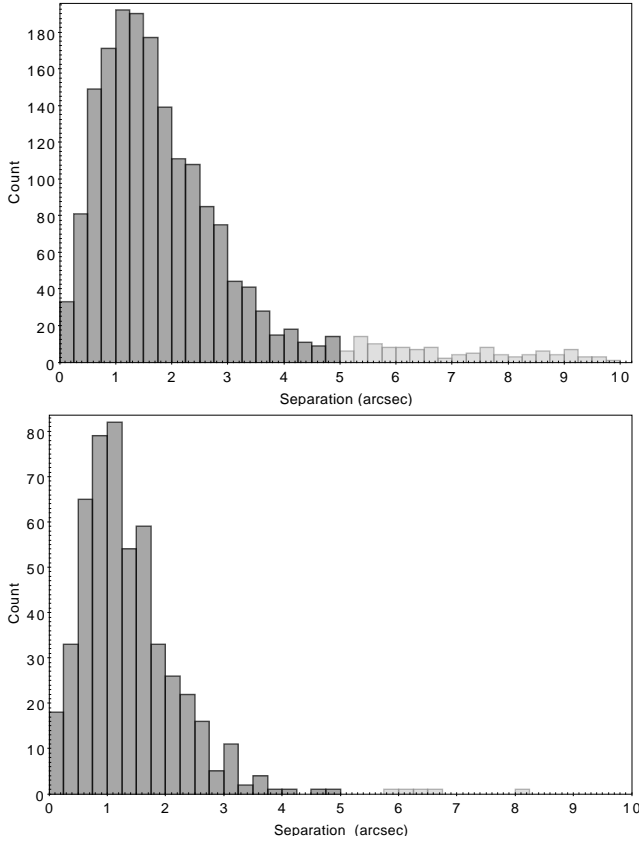


**Figure 1.** Angular offset (in arc seconds) between the locations of XCS point sources (with more than 300 background subtracted soft counts) and positions of AGN in the V13 (top) or SDSS-DR12Q (bottom) catalogues. Only those 1,316 AGN within 5 arcsec (dark shaded) of an XCS point source are included in the analyses herein (Sample-S0 in Table 1).

of the Galactic plane, 1,316 remained sources in our sample (Sample-S0 hereafter, see Table 1).

Redshifts for the AGN in Sample-S0 are taken from VC13 or from SDSS-DR12Q - if the AGN appears in both catalogues, the VC13 value was used (note that there is minimal difference in redshift for AGN appearing in both catalogues). Many of the AGN were detected in multiple XMM observations. A total of 2,649 XMM observations have been included in the analyses of Sample-S0 presented herein. The distributions of redshift for each AGN, off-axis angle and the full observation duration (i.e. before flare correction) of the 2,649 individual observations are shown in Figure 2.

### 3 DATA REDUCTION

#### 3.1 Extracting light curves

For each PN observation of the 1,316 AGN in Sample-S0, we generate a clean event list which takes into account flare cleaning according to the methodology of LD11. We note that, for this study, we use only PN detector data, because the other two EPIC camera detectors (MOS1 and MOS2) are less sensitive, especially in the soft, 0.5 – 2.0 keV, energy band.

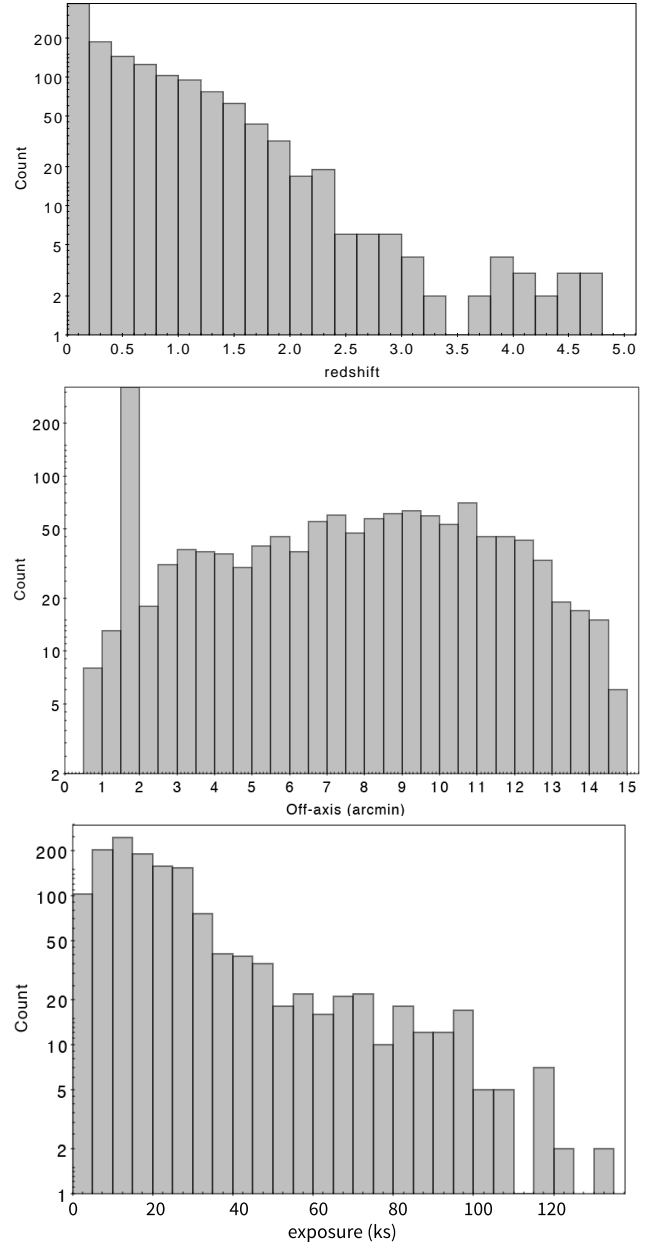


**Figure 2.** Properties of the 1,316 AGN in Sample-S0 (see Table 1). Top: Redshift distribution. Middle: Angular offset (arcmins) between the AGN location and the aim point of the respective XMM observation. Bottom: Full, i.e. before flare correction, XMM PN camera exposure time of the respective XMM observation.

We extracted, from the clean event list, the source light-curve from a circular region 20 arcsec in radius centred on the XAPA coordinates for each AGN. We extracted a background light-curve from a circular annulus, centred on the same coordinate, with inner and outer radii of 50 arcsec and 60 arcsec respectively. If other X-ray sources overlap with the source or background apertures, they were removed (“cheesed out”) using 20 arcsec radius circles. Figure 3 shows typical EPIC-PN images of AGN in our sample. The source extraction regions are defined by the solid green circles, and the background regions by the dashed green circles. The bottom



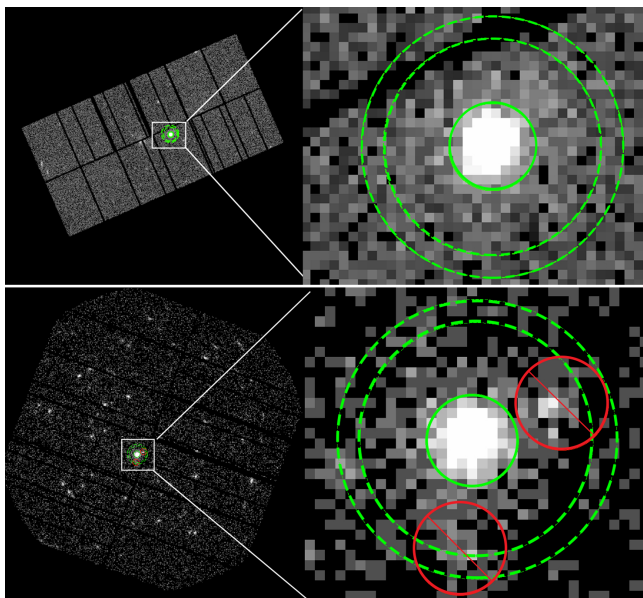


**Figure 3.** Top. PN ObsID 0673580301 and 16x zoomed in image of AGN XMMXCSJ132519.2-382455.2 (IRAS 13224-3809 in VC13), redshift 0.65. The image was created with a pixel size of 4.52 arcsec and within the energy range 2 – 10 keV. The inner solid green circle (radius 20'') defines the source region. The outer dashed green annulus (radii 50'' and 60'') defines the background region. Bottom. PN ObsID 0011830201 and 16x zoomed-in image of AGN XMMXCSJ152553.9+513649.3. Regions around nearby point sources, outlined in red, are masked from the regions used to define light curves and spectra.

image shows an AGN with two nearby point sources (red circles).

We then generated rest frame 0.3–10.0 keV source and background light-curves in the PN detector in 250s time bins using the XMM Science Analysis System (SAS) task EPICLCCORR. Figure 4 shows the background corrected light curves for the AGNs featured in Figure 3.

### 3.2 Spectral fitting and luminosity estimates

For each PN observation of the 1,316 AGN in Sample-S0, we extracted, from the clean event lists, spectra for each AGN from the same source and background regions used to generate the light-curves (§ 3.1).

The `arfgen` and `rmfgen` commands in SAS were used to generate the associated ancillary response files and detector matrices. The background-subtracted spectra were made such that there were a minimum of 20 counts in each channel. These were then fit in the 0.2 – 10.0 keV energy range, to a typical AGN model (e.g. Kamizasa et al. 2012):

`phabs*cflux(powerlaw + bbody)`

using XSPEC v12.8.2. The parameters in the `cflux` model are `Emin` and `Emax` (the minimum/maximum energy over which flux is calculated), set to 0.001 and 100.0 keV respectively, and `lg10Flux` (log flux in erg/cm<sup>2</sup>/s) which was left free. The other free parameters in our AGN model were the power-law index ( $\Gamma$ ), black body temperature and black

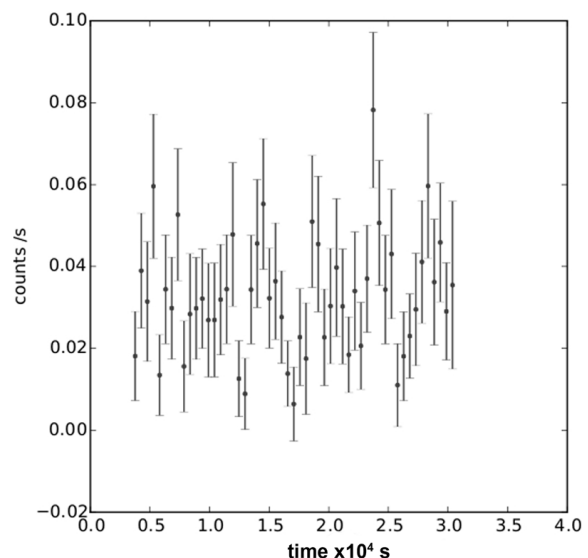
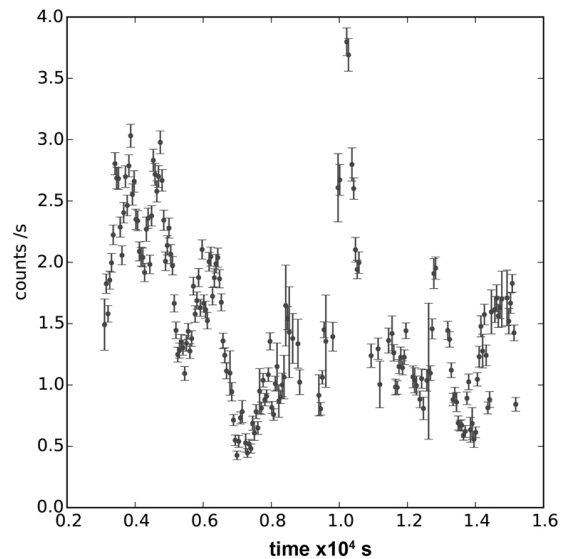


**Figure 4.** Background corrected light curves for AGN point-sources XMMXCSJ132519.2-382455.2 (top) and XMMXCSJ152553.9+513649.3 (bottom) taken from ObsID 0673580301 and 0011830201 respectively, with source and background regions extracted as Figure 3. The binsize is 250 seconds and the energy range is 0.3 – 10 keV.

body normalisation. We fixed the value of  $n_H$  to the value taken from Dickey & Lockman 1990

From the best fit model, we estimated the hard-band (2.0 – 10.0 keV) luminosity, and its 68.3 per cent confidence level upper and lower limits.

If the difference between the upper and lower limit on the luminosity ( $\Delta L_X$ ) was larger than the best fit value, i.e.  $\frac{\Delta L_X}{L_X} > 1$  then the respective AGN was excluded from further analyses. The remaining sample contained 1,091 AGN (making this the largest study of the X-ray spectral properties of AGNs) and is referred to as Sample-S1 hereafter (see Table 1). The median  $\frac{\Delta L_X}{L_X}$  of this sample is 0.16.

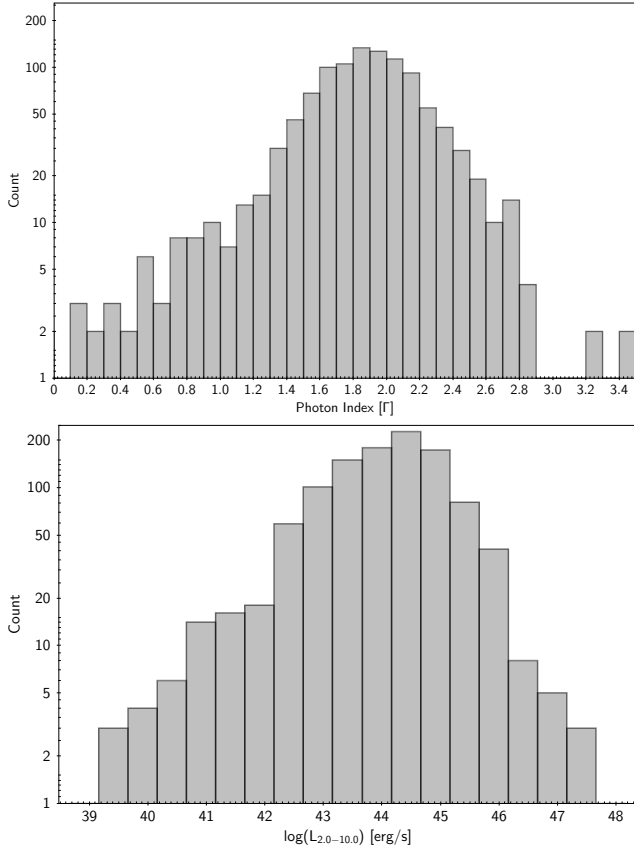


**Figure 5.** Histograms of the hard-band photon index  $\Gamma$  (top plot) and hard-band luminosity (bottom plot) for Sample-S1 (1091 AGN).

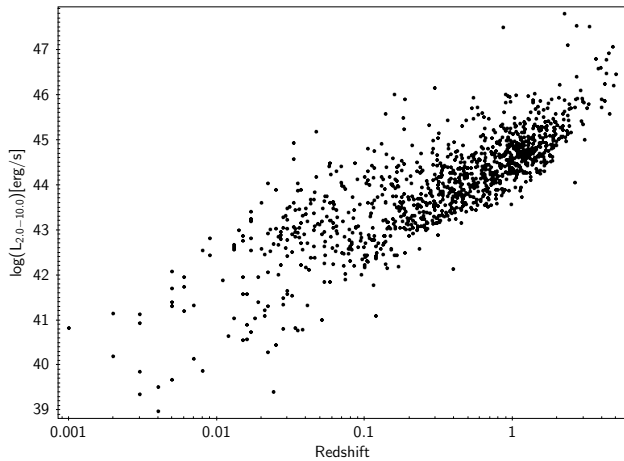


**Figure 6.** Distribution of Sample-S1 in the redshift-luminosity (hard band) plane.

Figure 5 (top), shows the distribution of power law index ( $\Gamma$ ) and the bottom plot shows the hard-band luminosity for Sample-S1. Where there are multiple observations of the same source, we used the value derived from the observation with the longest exposure time. Figure 6 shows the redshift distribution versus hard-band-luminosity for Sample-S1.

The average hard-band spectral index was measured to be  $\bar{\Gamma} = 1.81 \pm 0.34$ . This compares well with previous determinations. [Nandra & Pounds 1994](#) measured  $1.9 < \Gamma < 2.0$  using Ginga Large Area proportional Counter observations of 27 AGN. ([Corral et al. 2011](#)) found  $\bar{\Gamma} = 2.05 \pm 0.03$  using XMM observations of 305 AGN.

### 3.3 Determining normalised excess variance

The light-curves were divided into equal segments of 10 ks (then again into segments of 20 ks and 40 ks). As we used Gaussian statistics to derive a value of variability, we required a minimum of twenty time bins (of 250s duration) per light-curve segment. Each time bin within the segments were themselves required to have a minimum of 20 counts after correction for the effective fractional exposure (EFE). The EFE corrects for effects such as chip gaps and vignetting. Its value is stored in the `FRACEXP` parameter in the header of the background subtracted light-curve `.fits` file. Following the method of ([O’Neill et al. 2005](#)), any bin with `FRACEXP`  $< 0.35$  is rejected, even if the corrected counts is  $\geq 20$ . Again following ([O’Neill et al. 2005](#)), segments are rejected if they contain one or more bins with  $\leq 20$  where the fractional exposure is high (`FRACEXP`  $> 0.9$ ).

We also tested whether each of the light-curve segments for an individual AGN are in themselves *variable* by performing the chi-squared probability of constancy test included within the SAS task `EKSTEST`. Following ([Ponti et al. 2012](#)), we rejected any segment where the probability that the segment is not variable is  $> 0.01$ . The  $\sigma_{\text{NXS}}^2$  values for each AGN were then calculated using Equation 1 and a simplified version of Equation 4, i.e.

$$^* \sigma_{\text{NXS}}^2 = \sigma_{\text{NXS}}^2 (1+z)^{2\beta} \quad (5)$$

This simplification is possible because we measured  $\sigma_{\text{NXS}}^2$  in light-curve segments of consistent lengths, i.e. the  $(\Delta t^* / \Delta t_{\text{obs}})^{2\beta}$  term in Equation 4 is not needed. Hereafter we still use the term  $\sigma_{\text{NXS}}^2$ , rather than  $^* \sigma_{\text{NXS}}^2$  to describe normalized excess variance even after the  $(1+z)^{2\beta}$  correction has been applied. We rejected from further analysis any segments that yield negative values of  $\sigma_{\text{NXS}}^2$ , i.e. where the measurement uncertainty dominates the intrinsic variability (see § 1). We also rejected any segments where the  $\sigma_{\text{NXS}}^2$  error, as defined by Equation 3, is large, i.e. when  $\Delta \sigma_{\text{NXS}}^2 / \sigma_{\text{NXS}}^2 > 1$ . All remaining segments after these cuts are applied were labelled as *good*.

For each AGN we derived an unweighted mean value for  $\sigma_{\text{NXS}}^2$  from all *good* 10 ks (20 ks, 40 ks) light-curve segments. We calculated the  $1\sigma$  uncertainty on this mean value as<sup>3</sup>

$$\Delta \sigma_{\text{NXS}}^2 = \frac{\sigma_{\text{NXSmax}}^2 - \sigma_{\text{NXSmin}}^2}{2\sqrt{N_{\text{segs}}}}, \quad (6)$$

where  $\sigma_{\text{NXSmax}}^2$  and  $\sigma_{\text{NXSmin}}^2$  are the maximum and minimum variability values, and  $N_{\text{segs}}$  is the number of *good* 10 ks (20 ks, 40 ks) segments.

<sup>3</sup> e.g. [virgo-physics.sas.upenn.edu/uglabs/lab\\_manual/Error\\_Analysis.pdf](http://virgo-physics.sas.upenn.edu/uglabs/lab_manual/Error_Analysis.pdf)

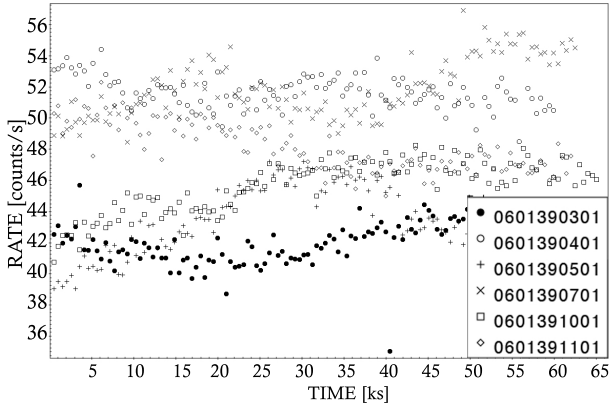


**Figure 7.** The PN detector light-curves in 250s bins of the AGN XMMXCSJ204409.7-104325.8 in ObsIDs 0601390301, 0601390401, 0601390501, 0601390701, 0601391001 and 0601391101 (0.5-10 keV).

### 3.4 Mitigation of red-noise

AGN exhibit a-periodic *red-noise*, whereby there is an inherent uncertainty in the long-term variability due to the stochastic nature of AGN emission. As a result, an AGN light-curve generated at a given epoch is just one of many manifestations of the light-curve that the AGN will exhibit over its lifetime (see Vaughan et al. 2003b). Estimating *red-noise* is difficult, as it depends on the steepness of the PSD of the AGN. Thus, uncertainty regarding *red-noise* would persist even if the measurement errors on a given  $\sigma_{\text{NXS}}^2$  could be reduced to zero. This is demonstrated in Figure 7, which shows light curves for an AGN that was observed by XMM at multiple epochs, the offset in the normalization between the six curves demonstrates the underlying stochastic variability. Figure 8 shows the respective  $\sigma_{\text{NXS}}^2$  value (across the duration of the observation rather than in 10, 20 or 40 ks segments) measured from these observations, with the x-axis showing the start of observation in XMM mission time. The dark and light grey shaded areas represent the 1 and  $2\sigma$  scatter regions relative to the best fit  $L_X$ - $\sigma_{\text{NXS}}^2$  [20ks] relation (as defined in Figure 10) at the mean  $L_X$  of this AGN (i.e. all the  $\sigma_{\text{NXS}}^2$  measurements are within  $2\sigma$  of the derived  $L_X$ - $\sigma_{\text{NXS}}^2$  relation.)

For our correlation analysis, we only included AGN with five or more *good* segments (see § 4.2.3 for a discussion of this approach). Figure 9 shows number of AGN with *good* 10 ks, 20 ks and 40 ks segments available from the AGNs in Sample-S1.

### 3.5 S10, S20, S40 sub-samples

From this approach we defined three different sub-samples as S10, S20 and S40. These contain 63, 41 and 20 AGN respectively. All  $L_X$ ,  $\sigma_{\text{NXS}}^2$  and  $\Gamma$  values derived for the AGN in these samples as well as  $M_{\text{BH}}$  from reverberation mapping studies and AGN type are combined in Table 7 in Appendix 6. These sub-samples were used to investigate the correlations between X-ray properties and  $M_{\text{BH}}$ .

With regard to  $M_{\text{BH}}$ , these values were taken from (Bentz & Katz 2015), using a cross match radius of 5 arcsec. The

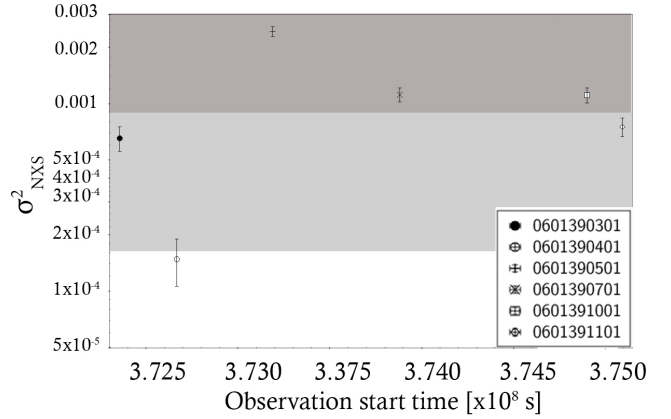


**Figure 8.** The measured  $\sigma_{\text{NXS}}^2$  value for the AGN XMMXCSJ204409.7-104325.8 using the lightcurves shown in Figure 7. The respective observation start time is indicated on the x-axis. For reference, we show the 1 and  $2\sigma$  (dark and light grey respectively) confidence regions relative to the best fit  $L_X$ - $\sigma_{\text{NXS}}^2$  [20ks] relation at the mean  $L_X$  for this AGN (see Figure 10).

number of (Bentz & Katz 2015) masses for each of the respective sub-samples are listed in Table 1. With regard to AGN type, these were taken primarily from VC13 (where AGN type is based on the appearance of the Balmer lines) and in the case of two not given in VC13, supplemented by information in the SIMBAD database of astronomical objects (Wenger et al. 2000). Accordingly; 52 of the 89 AGN in the table are classified solely as Type 1, six as Type 1.2, fifteen as 1.5, four as 1.8, one as 1.9 and one as Type 2. The rest are classified as BL (Blazars) and Q (Quasars i.e. a high luminosity and redshift AGN), see § 5.1 for a discussion.

## 4 CORRELATIONS BETWEEN X-RAY PROPERTIES AND WITH BLACK HOLE MASS

### 4.1 Results

We used the regression method of (Kelly 2007) to derive the relationships between: *i*) hard-band luminosity and normalised excess variance (Figure 10 and Table 3), *ii*) normalised excess variance and black hole mass (Figure 11, Table 4), and *iii*) hard-band luminosity and black hole mass (12, Table 5). Significant correlations can be seen in all cases. There is a negative correlation between  $\sigma_{\text{NXS}}^2$  and  $L_X$ , i.e. brighter AGN are less variable. There is also a negative correlation between  $\sigma_{\text{NXS}}^2$  and  $M_{\text{BH}}$ , i.e. more massive black holes are surrounded by less variable AGN. Not surprisingly, therefore, there is a positive correlation between  $L_X$  and  $M_{\text{BH}}$ , i.e. brighter AGN contain more massive black holes. Our results are consistent with previous studies that have demonstrated an anti-correlation between luminosity and variability, e.g. (Lawrence & Papadakis 1993), (Barr & Mushotzky 1986), (O'Neill et al. 2005), (Ponti et al. 2012). It is not appropriate to compare slopes, scatter and normalisation with published results because of our differing ap-

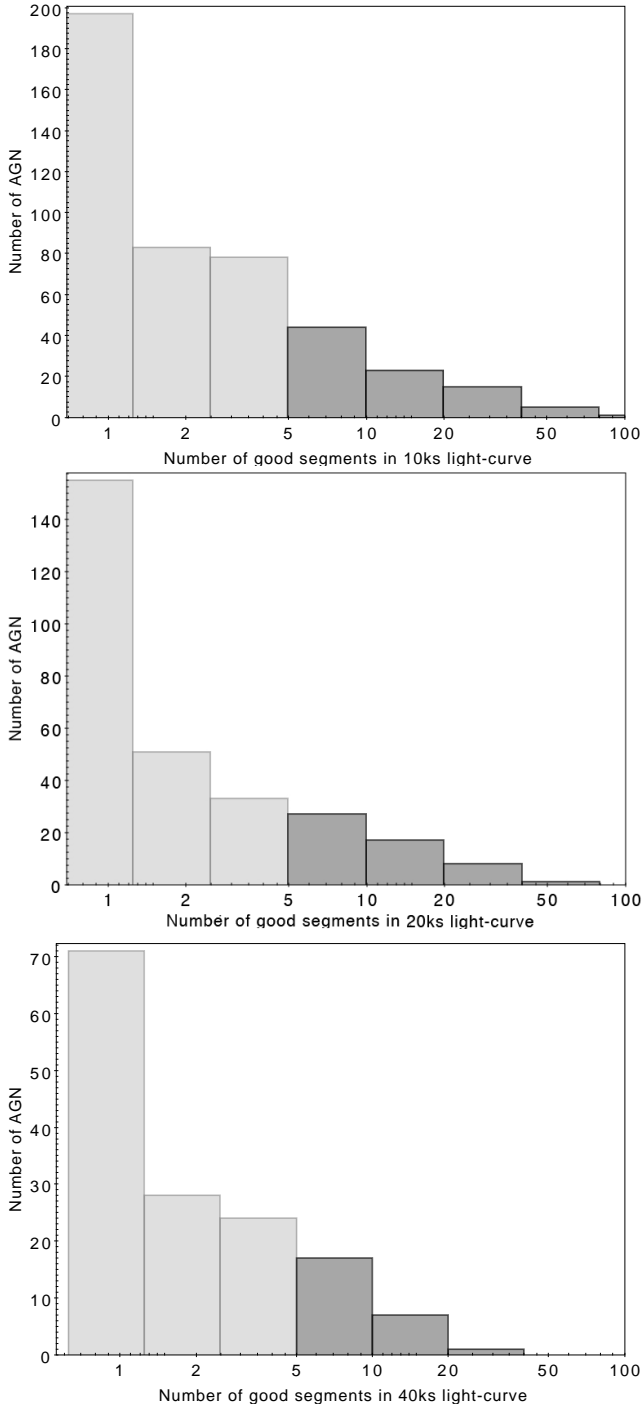


**Figure 9.** Histogram of the number of AGN with *good* 10 ks (top), 20 ks (middle) and 40 ks (bottom) segments from our Sample-S1. The dark bars are for AGN with five or more segments.

proach to fitting. Instead, we applied our fitting method to the variability and  $L_X$  data in (Ponti et al. 2012), see Figure 13. We note that what we call  $\sigma_{\text{NXS}}^2[20\text{ks}]$ , they define as  $s_{20}$ , albeit with a different approach to error estimation. The fitting results are compared in Table 3 and show an excellent agreement with those shown in the middle panel of Figure 10.

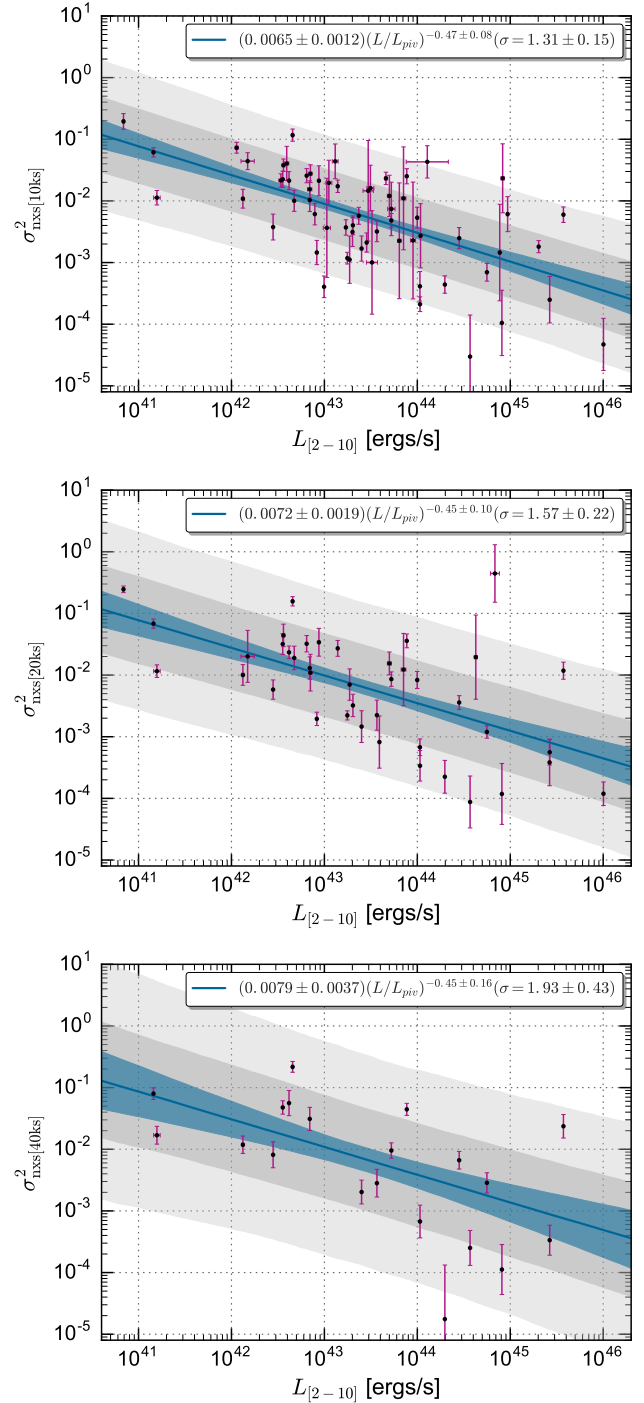


**Figure 10.**  $L_X$  plotted against  $\sigma_{\text{NXS}}^2$  where there are five or more *good* 10 ks (top), 20 ks (middle), 40 ks (bottom) light-curve segments for each AGN. Blue line is the best fit relation with 1- $\sigma$  uncertainty. Grey regions are 1 and 2- $\sigma$  scatter.

#### 4.1.1 Test for redshift evolution

We also tested for evidence of redshift evolution in the scaling relations. The method assumes a null hypothesis that there is no redshift evolution. We then added an evolution factor,  $E(z)^\alpha$  (where  $E^2(z) = \Omega_M(1+z)^3 + \Omega_\Lambda$ ), and look for a model which gives us the smallest intrinsic scatter. For



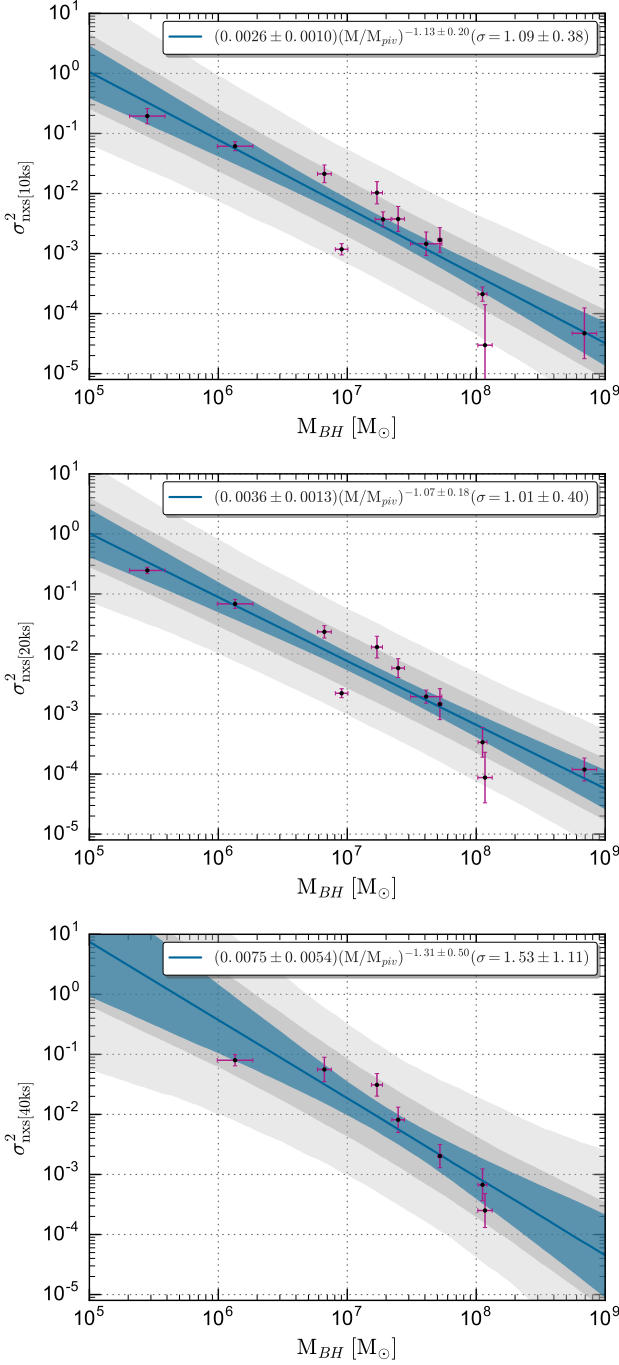


**Figure 11.** Black hole masses from reverberation mapping studies as catalogued in (Bentz & Katz 2015) plotted against  $\sigma_{\text{NXS}}^2$  10 ks (top), 20 ks (middle) and 40 ks (bottom) segment light-curves. Blue line is the best fit relation with 1- $\sigma$  uncertainty. Grey regions are 1 and 2- $\sigma$  scatter. ( $M_{\text{piv}} = 2 \times 10^7 M_{\odot}$ ).

each value of  $\alpha$  we ran an MCMC fitting. Then we compare it with our null hypothesis to see if the intrinsic scatter has decreased with the addition of the extra term.

In none of the cases tested, i.e.  $L_X$  and  $\sigma_{\text{NXS}}^2$  (in samples S10, S20 and S40), black hole mass and  $\sigma_{\text{NXS}}^2$  (in samples S10, S20 and S40) and black hole mass and  $L_X$  (sample S1), do we find statistically significant evidence for decreasing

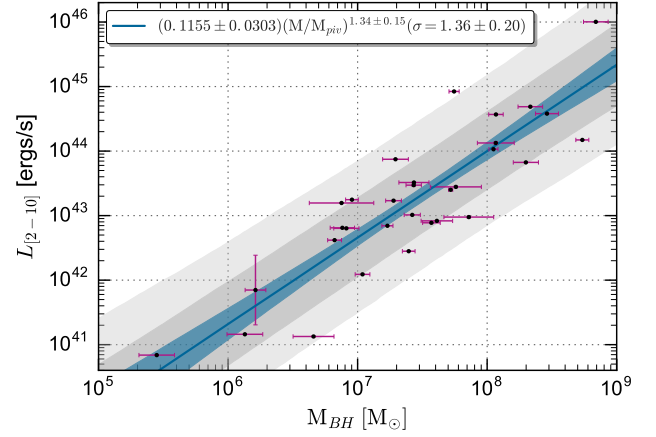


**Figure 12.** Black Hole masses from reverberation mapping studies as catalogued in (Bentz & Katz 2015) plotted against hard-band luminosity. Blue line is the best fit relation with 1- $\sigma$  uncertainty. Grey regions are 1 and 2- $\sigma$  scatter. ( $M_{\text{piv}} = 2 \times 10^7 M_{\odot}$ )

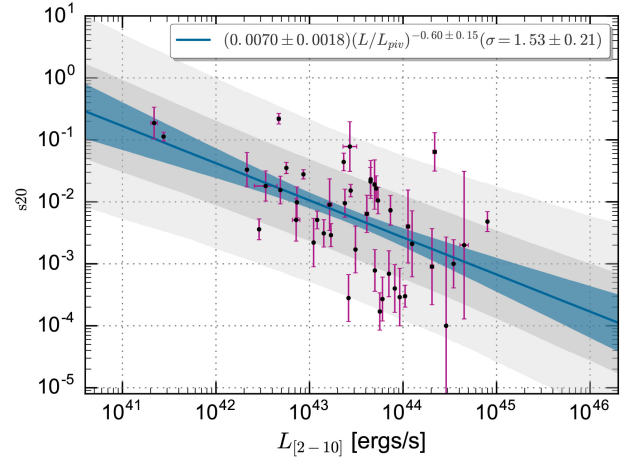


**Figure 13.** hard-band luminosities from (Bianchi et al. 2009b) plotted against s20 (equivalent to our  $\sigma_{\text{NXS}}^2$  [20ks] term) for 45 AGN in the CAIXA survey (Ponti et al. 2012) Blue line is the best fit relation with 1- $\sigma$  uncertainty. Grey regions are 1 and 2- $\sigma$  scatter. ( $L_{\text{piv}} = 2 \times 10^{43} \text{ erg s}^{-1}$ ).

scatter. We conclude that our data are consistent with a ‘no redshift evolution’ model. It is worth noting the following; i) our null hypothesis, i.e. no redshift evolution, is an arbitrary choice; ii) we are limited by the statistical power of the sample, hence if we have a larger sample size we may find evidence of an evolutionary trend; iii) masses are all taken from reverberation mapped AGN at  $z < 0.24$ , therefore the redshift baseline to test for evolution is not very large; iv) there may be a further issue related to our source selection, i.e. the lack of low luminosity AGN in our sample at high redshift (see Figure 6). As this is the first attempt to look at evolution in the  $L_X$ ,  $\sigma_{\text{NXS}}^2$  and  $M_{\text{BH}}$  relations in this way, we cannot compare our findings against previous results.

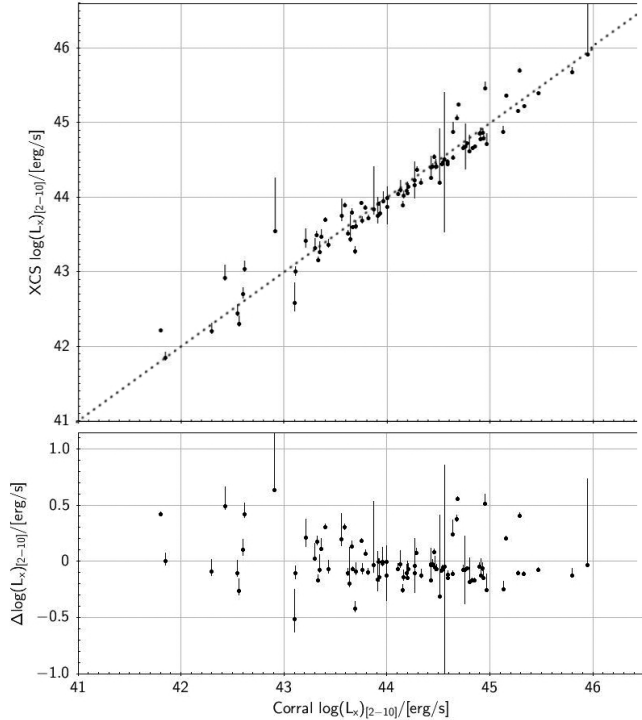


**Figure 14.** Hard-band (2.0-10 keV) luminosity of 78 AGN in Sample-S1 common with (Corral et al. 2011). The dotted line shows the one-to-one relation (x-axis error bars are not shown for the Corral  $L_X$  estimates as these are not included in their table of results).

## 4.2 Methodology tests

We carried out several tests to explore the robustness of the results presented in Section 4.

### 4.2.1 Luminosity

We compared our hard-band luminosity results with those estimated by (Corral et al. 2011), a X-ray spectral analysis of  $> 300$  AGN ( $z < 2.4$ ) belonging to the XMM-Newton bright survey (XBS). There are 78 AGN in common with our S1 sample. We found good agreement between the two sets of  $L_X$  measurements, see Figure 14.

### 4.2.2 Normalised excess variance

We compared our values for  $\sigma_{\text{NXS}}^2$  with those of the (Ponti et al. 2012) CAIXA survey. There are 98 AGN in common with our S1 sample. Of these, there are 19 AGN in the S20 samples (i.e. with five or more good 20 ks light-curve segments). We found a good agreement between our  $\sigma_{\text{NXS}}^2[20\text{ks}]$  results and the equivalent  $s_{20}$  values from (Ponti et al. 2012), see Figure 15.

### 4.2.3 Choice of minimum number of light-curve segments

The results presented in Table 3 were based on setting the minimum number of *good* light-curve segments to five. This

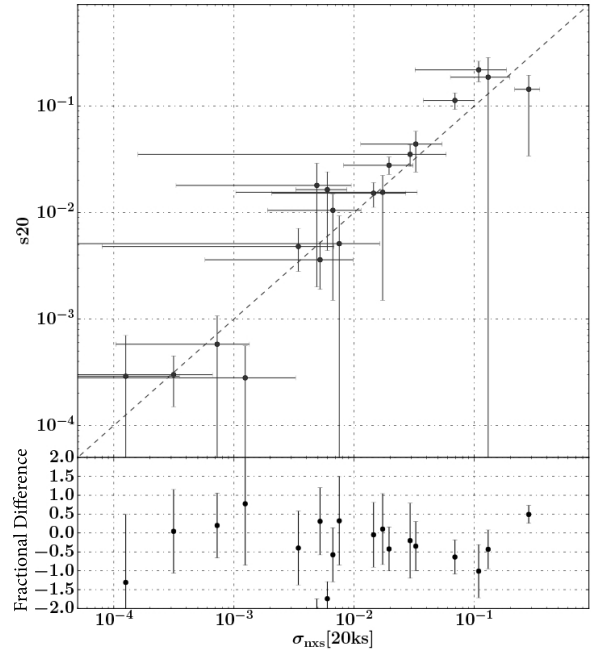


**Figure 15.** Comparison between CAIXA  $s_{20}$  and our  $\sigma_{\text{NXS}}^2$  over 20 ks with five or more good light-curve segments (Sample-S20). Dotted line is the one-to-one relation.

is a somewhat arbitrary choice. Setting a lower minimum would have allowed us to include more AGN in the fits. Setting a higher minimum would have increased the precision on the individual measurements.

Therefore, we investigated how the fit to the  $L_X$  to  $\sigma_{\text{NXS}}^2$  relation changed with the minimum number of light-curve segments (from 2 to 10) for both  $\sigma_{\text{NXS}}^2[10\text{ks}]$  and  $\sigma_{\text{NXS}}^2[20\text{ks}]$ . Although no significant effect was found to the relation, decreasing the number of segments increases the uncertainty - as shown in Figure 16 - and hence five was chosen as an optimal number.

### 4.2.4 Luminosity contamination by line-of-sight clusters

We checked to see if any of our AGN lies within or along the line-of-sight to a galaxy cluster. If this was the case, emission from the cluster might boost the measured  $L_X$  of the AGN. We cross matched all the AGN positions in our S0-Sample with extended XCS sources that been identified as a cluster in the redMaPPer SDSS DR8 cluster catalogue (Rykoff et al. 2014). For this we used a matching radius of  $\sim 250$  kpc, assuming the redshift in the redMaPPer catalogue. We found 12 matches (i.e.  $\sim 1$  per cent of sample S1), one of which is shown in Figure 17. None of these 12 were included in the scaling relations presented in § 4 as in all cases there were fewer than five *good* light-curve segments.

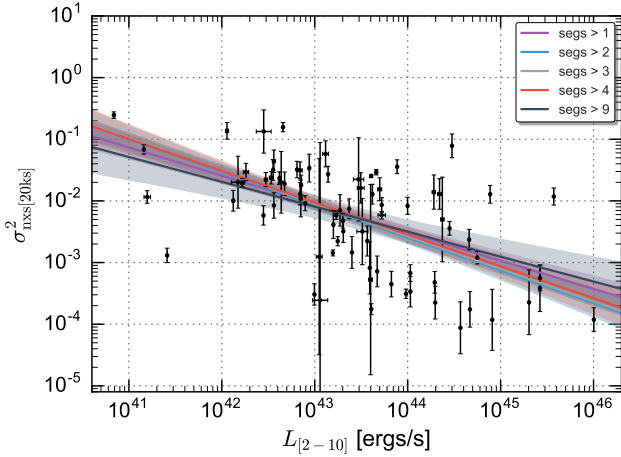


**Figure 16.**  $L_X$  plotted against 20 ks  $\sigma_{\text{NXS}}^2$  showing how the best fit relation changes when we change the number of 20 ks segments included in our sample. (For clarity, only the data points for  $> 2$  segments are shown). Uncertainties on  $\sigma_{\text{NXS}}^2$  were calculated using Equation. 6.

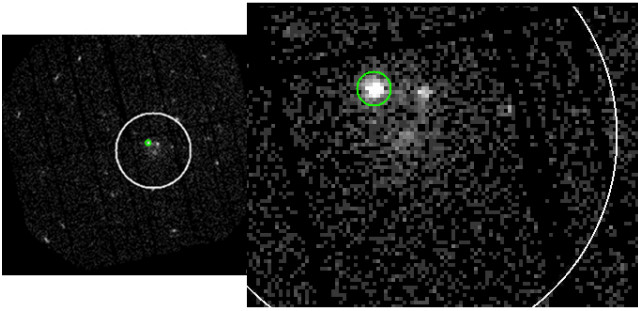


**Figure 17.** PN observation 0305920401 and zoomed image of AGN XMMXCSJ143450.6+033842.5 (green circle). This AGN at  $z = 0.028$  is within the projected 250 kpc core radius (white circle) of a redMaPPer cluster with a separation of 63 arcsec. The cluster is at  $z = 0.146$  at which redshift the angular extent of the core region is 97 arcsec. The pixel size  $4.52''$  in energy range 0.5 – 2.0 keV.

### 4.3 Expectations for eROSITA luminosity measurements

The eRASS exposure time is dependent on ecliptic latitude ( $lat$ ). According to (Merloni et al. 2012), the approximate exposure time  $T_{\text{EXP}}$  is given by:  $T_{\text{EXP}} \sim 1627 / \cos(lat)$  seconds for  $-84^\circ < lat < 84^\circ$  and  $T_{\text{EXP}} \sim 17,500$  seconds within  $6^\circ$  of the each ecliptic pole. This assumes 100 per cent observing efficiency. A more realistic efficiency is 80 per cent. These predictions refer to the full four year survey. The exposure time for each of the eight all-sky surveys, will be 8 times lower, so of the order of hundreds of seconds on average. Therefore, it will be impossible to measure  $\sigma_{\text{NXS}}^2$  values from the majority of eRASS data. However, it will still be possible to estimate  $L_X$  values. We forecast the accuracy of the eRASS derived  $L_X$  values below.

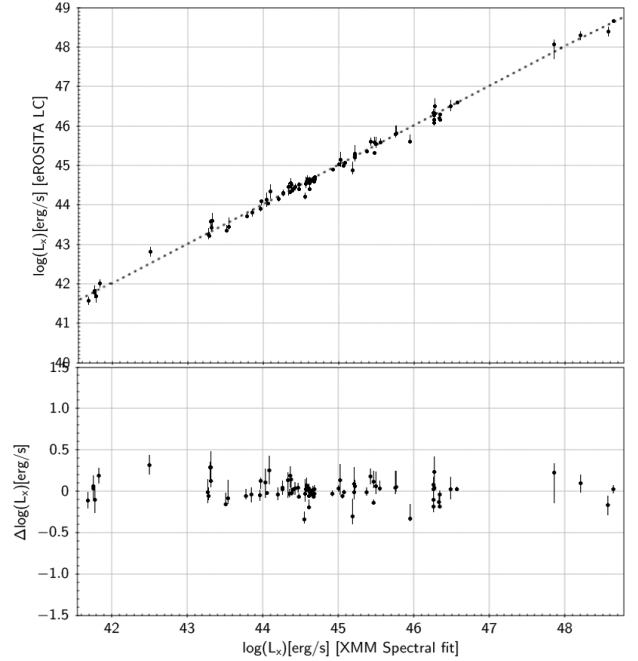


**Figure 18.** Comparison of the 2-10 keV luminosity derived from spectral fitting to the XMM full exposure time observations to the luminosities fit to an estimated eROSITA observation time for 80 observations of 44 AGN. The dotted line shows the one-to-one relation

#### 4.3.1 eRASS $L_X$ from spectral fits

If the AGN flux is sufficiently high, it will be possible to estimate  $L_X$  from the eRASS data using spectral fitting. To predict the accuracy of such fits, we have used the existing XMM observations of AGN in Sample-S1 and selected 2-10 keV light-curve segments at random, with a duration of the likely eROSITA exposure time in one of the eight All Sky Surveys. The exposure time was adjusted respective to the AGN latitude. For this exercise we continued to use XMM calibration files, but scaled the exposure time by the ratio of the XMM:eRASS sensitivity (from a comparison of respective effective area in the 2-10 keV energy range, the combined effective area of the seven eROSITA detectors is a factor of about 3.2 less than the XMM PN detector, Merloni et al. 2012). We extracted source and background spectra for these light-curve segments, and then fit the absorbed powerlaw models as described in Section 3.2. From these fits we extracted  $L_X$  and  $\Delta L_X$  values.

Of the 1091 AGN from 1753 XMM observations tested, successful spectral fits were derived in only 172 cases, corresponding to 98 unique AGN. Of these, there were 80 fits (44 unique AGN) where  $\frac{\Delta L_X}{L_X} < 1$ . The results from these 80 fits are compared to those derived from the full XMM exposure time in Figure 18. There is excellent agreement albeit only for the  $\simeq 4\%$  highest flux AGN.

#### 4.3.2 eRASS $L_X$ from count-rates

Where the AGN flux is not high enough to yield a meaningful spectral fit, then it is still possible to estimate  $L_X$  from the source count-rate using an assumed spectral model. For

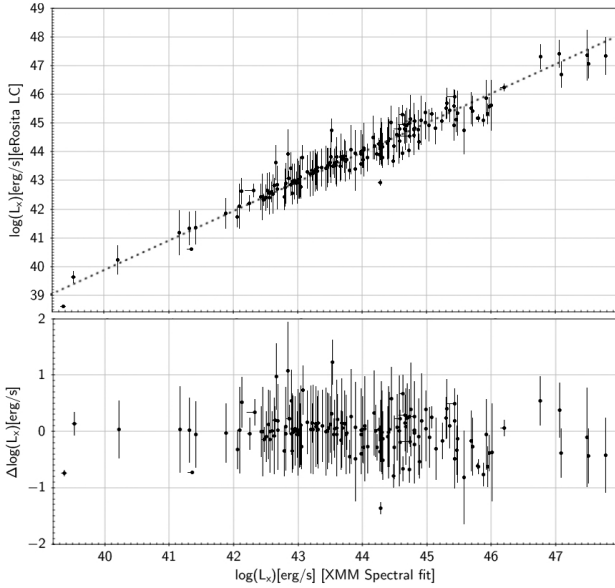


**Figure 19.** Comparison of the 2-10 keV luminosity derived from spectral fitting from actual XMM full observation time with fitting from the light-curve method 154 AGN. The dotted line shows the one-to-one relation

this exercise, we used an absorbed powerlaw (with  $\Gamma = 1.7$ ), with an  $n_H$  value appropriate for the respective AGN galactic latitude. The conversion factors between count-rate and luminosity were generated using XSPEC. For this test we used 254 on-axis observations of 154 AGN.

To predict an  $L_X$  value for a typical eRASS observation duration, we chose a random start time in the respective observations and set the light-curve duration to be the typical eROSITA observation time at that latitude with a scaling to account for the difference in the XMM:eROSITA sensitivity as used above (Section 4.3.1). A background subtracted light-curve was extracted in the 2-10 keV range and the count-rate recorded. We repeated eight times (to mimic the eight eRASS passes) and calculated the mean and error on the mean. These were then converted to  $L_X$  using the scaled XSPEC generated conversion factors. (We note that the error on the mean is likely to be an underestimate since the eight light curves came from the same observation rather than eight different epoch observations as would be the case with eRASS). All 254 observations provided an estimate for  $L_X$ .

Figure 19 shows a comparison between  $L_X$  derived from the full-observation spectral method and from this count-rate method (where there were two or more observations of the same AGN, we took the most recent for the count-rate  $L_X$  comparison).

We plot the  $M_{BH}$  to  $L_X$  relation for luminosity derived this way and find that the relation is statistically similar to the relation of  $M_{BH}$ - $L_X$  from a spectroscopic analysis of full XMM observations, albeit with larger uncertainty. This is shown in Figure 20 with correlation shown in Table 5.

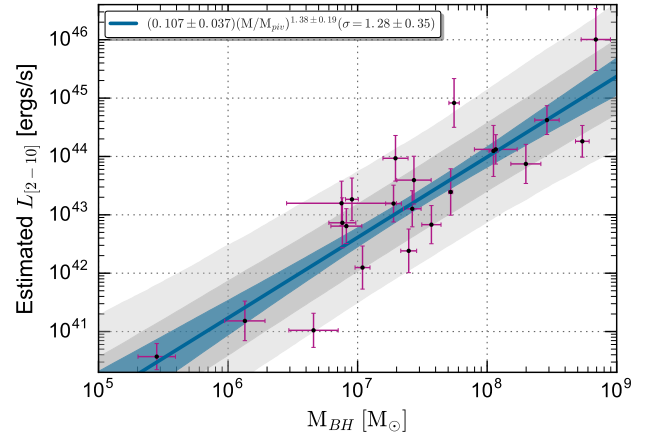


**Figure 20.** Black Hole masses from reverberation mapping studies as catalogued in (Bentz & Katz 2015) plotted against hard-band luminosity estimated from the count-rate of eight passes of typical eROSITA exposure duration ( $M_{piv} = 2 \times 10^7 M_\odot$ ). Blue line is the best fit relation with 1- $\sigma$  uncertainty. Grey regions are 1 and 2- $\sigma$  scatter.

## 5 DISCUSSION

### 5.1 AGN Type

Our calculations of  $L_X$  assumed that the emission from the AGN is isotropic. This is valid if the emission is not beamed but should be taken into account otherwise. Viewing angle will also have an effect on the line-of-sight hydrogen column density, with Type 2 having higher intrinsic values than Type 1. Therefore, an estimate of the absorption at the location of the AGN itself should be combined with the  $n_H$  value (e.g. from Dickey & Lockman 1990) when the fitting the model.

However, the relationship derived between  $L_X$  and  $M_{BH}$  shown in Figure 12 and Table 5 is based only on Type 1 AGN (these are the only ones for which reverberation mapping mass estimates can be made). Therefore, AGN type should not be an issue. That said, when using eRASS  $L_X$  as a proxy for  $M_{BH}$ , one would need to take into account the impact of mixing AGN types. This should not be a problem because spectra will be needed to secure redshifts, and those same spectra can be used to determine AGN type. (A large fraction of the eRASS AGN are planned to be observed by the 4MOST<sup>4</sup> spectrograph.)

### 5.2 Selection effect at high redshift

We see from Figure 6 that there is a clear trend of increasing  $L_X$  with redshift in sample S1 due to the flux limited nature of the observations. Therefore there may be selection effects that have not so far been taken into account within our correlations involving  $L_X$ . Further selection effects may also be involved for relations involving  $M_{BH}$ , as the reverberation-mapped masses are available only for the brightest AGN at relatively low- $z$  ( $z < 0.24$  in our study).

<sup>4</sup> www.4most.eu



### 5.3 Expanding the sample size

We have based our  $M_{\text{BH}}$  to  $\sigma_{\text{NXS}}^2$  and  $M_{\text{BH}}$  to  $L_X$  relationship on only  $\sim 30$  Type 1 AGN at  $z < 0.24$ , because these were the only AGN available to us that had  $M_{\text{BH}}$  measurements from reverberation mapping. In future work, we will extend our analysis by including other types of  $M_{\text{BH}}$  measurements e.g. from the luminosity and the width of the broad H $\alpha$  line. For example, there are a  $\sim 220$  AGN in our S1 sample where  $M_{\text{BH}}$  has been estimated in (Shen et al. 2008) based on H $\beta$ , Mg II, and C IV emission lines.

We can also extend our sample by drawing on new compilations of reverberation mapping  $M_{\text{BH}}$  measurements. In particular, we look forward to measurements from the OzDES project (Tie et al. 2016). This project is targeting AGN in the Dark Energy Survey deep fields. It aims to derive reverberation mapped  $M_{\text{BH}}$  for  $\sim 500$  AGN over a redshift range of  $0 < z < 4$ , with 3 per cent uncertainty. Cross-matching the OzDES target list with Sample S1, we found 35 AGN in common. Of these, fifteen were not already included in Figure 12. In Table 6, we present  $L_X$  values for these 15 derived by following the same spectral fitting methodology as before and these are shown in Table 6.

We note that late in the preparation of this manuscript, a sample of 44 new  $M_{\text{BH}}$  measurements was published (Grier et al. 2017). However, only one of these was new to our S1 sample.

## 6 SUMMARY

In this paper we used AGN associated with XCS point sources to confirm the existence of scaling relations between  $M_{\text{BH}}$ ,  $L_X$  and with  $\sigma_{\text{NXS}}^2$ . With our sample, we found no significant redshift evolution of these scaling relations demonstrating the potential to apply the relations over a wider redshift range than previously used.

We have described a method to estimate the  $L_X$  of an AGN from count-rates of short duration observations where  $\sigma_{\text{NXS}}^2$  cannot be measured. We have shown that although the uncertainties on the count-rate derived  $L_X$  are larger than spectrally derived  $L_X$ , the scaling relation with  $M_{\text{BH}}$  is the statistically similar. This will be particularly relevant to future X-ray missions such as eROSITA where short observations allow us to estimate potentially tens of thousands of  $M_{\text{BH}}$  from this scaling relation.

We have estimated that our sample of AGN with both XCS derived  $L_X$  values, and with reverberation mapping derived  $M_{\text{BH}}$  estimates, will be increased by up to 50% once the OzDES survey starts providing new reverberation mapped data of AGN.

## ACKNOWLEDGEMENTS

JM acknowledges support from MPS, University of Sussex. KR acknowledges support from the Science and Technology Facilities Council (grant number ST/P000252/1). MS acknowledges support by the Olle Engkvist Foundation (Stiftelsen Olle Engkvist Byggmästare). MH acknowledges financial support from the National Research Foundation, the South African Square Kilometre Array project, and the University of KwaZulu-Natal.

## REFERENCES

- Antonucci M., Vagnetti F., Trevese D., 2014, in *The X-ray Universe 2014*. p. 222
- Barr P., Mushotzky R. F., 1986, *Nature*, **320**, 421
- Bentz M. C., Katz S., 2015, *PASP*, **127**, 67
- Bianchi S., Guainazzi M., Matt G., Fonseca Bonilla N., Ponti G., 2009a, *A&A*, **495**, 421
- Bianchi S., Bonilla N. F., Guainazzi M., Matt G., Ponti G., 2009b, *A&A*, **501**, 915
- Blandford R. D., McKee C. F., 1982, *ApJ*, **255**, 419
- Corral A., Della Ceca R., Caccianiga A., Severgnini P., Brunner H., Carrera F. J., Page M. J., Schwope A. D., 2011, *A&A*, **530**, A42
- Di Matteo T., 2001, *X-ray Astronomy: Stellar Endpoints, AGN, and the Diffuse X-ray Background*, 599, 83
- Dickey J. M., Lockman F. J., 1990, *ARA&A*, **28**, 215
- Elvis M., Maccacaro T., Wilson A. S., Ward M. J., Penston M. V., Fosbury R. A. E., Perola G. C., 1978, *MNRAS*, **183**, 129
- Ferrarese L., 2002, *ApJ*, **578**, 90
- Ferrarese L., Ford H., 2005, *Space Sci. Rev.*, **116**, 523
- Ferrarese L., Merritt D., 2000, *ApJ*, **539**, L9
- Gandhi P., 2005, *Asian Journal of Physics*, **13**, 90
- Gebhardt K., et al., 2000, *ApJ*, **539**, L13
- George I. M., Turner T. J., Yaqoob T., Netzer H., Laor A., Mushotzky R. F., Nandra K., Takahashi T., 2000, *ApJ*, **531**, 52
- Ghez A. M., Salim S., Hornstein S. D., Tanner A., Lu J. R., Morris M., Becklin E. E., Duchêne G., 2005, *ApJ*, **620**, 744
- González-Martín O., Vaughan S., 2012, *A&A*, **544**, A80
- Grier C. J., et al., 2012, *ApJ*, **755**, 60
- Grier C. J., et al., 2017, preprint, ([arXiv:1711.03114](https://arxiv.org/abs/1711.03114))
- Kamizasa N., Terashima Y., Awaki H., 2012, *ApJ*, **751**, 39
- Kara E., 2018, in *American Astronomical Society Meeting Abstracts #231*. p.#422.01
- Kaspi S., Smith P. S., Netzer H., Maoz D., Jannuzi B. T., Giveon U., 2000, *ApJ*, **533**, 631
- Kelly B. C., 2007, *ApJ*, **665**, 1489
- Kelly B. C., Treu T., Malkan M., Pancoast A., Woo J.-H., 2013, *ApJ*, **779**, 187
- Körding E. G., Migliari S., Fender R., Belloni T., Knigge C., McHardy I., 2007, *MNRAS*, **380**, 301
- Kozłowski S., 2016, preprint, ([arXiv:1609.09489](https://arxiv.org/abs/1609.09489))
- Lawrence A., Papadakis I., 1993, *ApJ*, **414**, L85
- Lawrence A., Watson M. G., Pounds K. A., Elvis M., 1985, *MNRAS*, **217**, 685
- Lloyd-Davies E. J., et al., 2011, *mnras*, **418**, 14
- Ludlam R. M., Cackett E. M., Gültekin K., Fabian A. C., Gallo L., Miniutti G., 2015, *MNRAS*, **447**, 2112
- Magorrian J., et al., 1998, *AJ*, **115**, 2285
- Markowitz A., et al., 2003, *ApJ*, **593**, 96
- McHardy I., 1988, *Mem. Soc. Astron. Italiana*, **59**, 239
- McHardy I. M., Koerding E., Knigge C., Uttley P., Fender R. P., 2006, *Nature*, **444**, 730
- Merloni A., et al., 2012, preprint, ([arXiv:1209.3114](https://arxiv.org/abs/1209.3114))
- Middei R., Vagnetti F., Antonucci M., Serafinelli R., 2016, *Journal of Physics Conference Series*, **689**, 012006
- Nandra K., Pounds K. A., 1994, *MNRAS*, **268**, 405
- Nandra K., George I. M., Mushotzky R. F., Turner T. J., Yaqoob T., 1997, *ApJ*, **476**, 70
- O'Neill P. M., Nandra K., Papadakis I. E., Turner T. J., 2005, *MNRAS*, **358**, 1405
- Pan H.-W., Yuan W., Zhou X.-L., Dong X.-B., Liu B., 2015, *ApJ*, **808**, 163
- Papadakis I. E., 2004, *MNRAS*, **348**, 207
- Peterson B. M., Wanders I., Bertram R., Hunley J. F., Pogge R. W., Wagner R. M., 1998, *ApJ*, **501**, 82

- Ponti G., Papadakis I., Bianchi S., Guainazzi M., Matt G., Uttley P., Bonilla N. F., 2012, *A&A*, **542**, [A83](#)
- Pounds K. A., McHardy I. M., 1988, in Tanaka Y., ed., *Physics of Neutron Stars and Black Holes*. pp 285–299
- Predehl P., et al., 2010, in *Space Telescopes and Instrumentation 2010: Ultraviolet to Gamma Ray*. p. 77320U ([arXiv:1001.2502](#)), doi:10.1117/12.856577
- Rees M. J., 1984, *ARA&A*, **22**, 471
- Romer A. K., Viana P. T. P., Liddle A. R., Mann R. G., 2001, *ApJ*, **547**, [594](#)
- Rykoff E. S., et al., 2014, *ApJ*, **785**, [104](#)
- Sambruna R. M., Eracleous M., Mushotzky R. F., 1999, *ApJ*, **526**, [60](#)
- Shen Y., Greene J. E., Strauss M. A., Richards G. T., Schneider D. P., 2008, *ApJ*, **680**, [169](#)
- Sijacki D., Springel V., Di Matteo T., Hernquist L., 2007, *MNRAS*, **380**, [877](#)
- Tie S. S., et al., 2016, preprint, ([arXiv:1611.05456](#))
- Tremaine S., et al., 2002, *ApJ*, **574**, [740](#)
- Trujillo I., Graham A. W., Caon N., 2001, *MNRAS*, **326**, [869](#)
- Uttley P., McHardy I. M., Papadakis I. E., 2002, *MNRAS*, **332**, [231](#)
- Vaughan S., Fabian A. C., Nandra K., 2003a, *MNRAS*, **339**, [1237](#)
- Vaughan S., Edelson R., Warwick R. S., Uttley P., 2003b, *MNRAS*, **345**, [1271](#)
- Veron-Cetty M. P., Veron P., 2010, *VizieR Online Data Catalog*, **7258**
- Vestergaard M., 2002, *ApJ*, **571**, [733](#)
- Watson M. G., et al., 2009, *A&A*, **493**, [339](#)
- Wenger M., et al., 2000, *A&AS*, **143**, [9](#)
- Zhou X.-L., Zhang S.-N., Wang D.-X., Zhu L., 2010, *ApJ*, **710**, [16](#)
- van der Klis M., 1997, in Babu G. J., Feigelson E. D., eds, *Statistical Challenges in Modern Astronomy II*. p. 321 ([arXiv:astro-ph/9704273](#))

Sample (1)	Description (2)	No. (3)
Initial	XCS sources in VC13 and/or SDSS-DR12Q	2039 <sup>1</sup> (46)
S0	AGN $b > 10^\circ$	1316 (38)
S1	S0 and $L_X$ value where $\frac{\Delta L_X}{L_X} < 1$	1091 (31)
S10	S1 and $\geq 5$ 10 ks light-curve segments	63 (12)
S20	S1 and $\geq 5$ 20 ks light-curve segments	41 (11)
S40	S1 and $\geq 5$ 40 ks light-curve segments	20 (7)

**Table 1.** Summary of the AGN samples used in the analysis. (1) sample name, (2) defines how the sample was filtered, (3) the number of AGN in the sample and in brackets the number with masses from reverberation mapping. <sup>1</sup>1689 from VC13, 513 from DSDSS-DR12Q with 163 common to both.

Survey (1)	Detector (2)	Type (3)	No. (4)	10 ks segs (5)	20 ks segs (6)	40 ks segs (7)	z (8)
This analysis	XMM	Targeted and serendipitous	1316	288 (63)	199 (41)	84 (20)	0.001-4.9
(Ponti et al. 2012)	XMM	Radio quiet targeted	161	51	58	45	0.001-4.52
(O’Neill et al. 2005)	ASCA	Radio quiet targeted	68			46	0.001-0.234
(Zhou et al. 2010)	XMM/ASCA	Reverberation mapped AGN	21			21	0.001-0.14

**Table 2.** Comparison between our survey sample and previous similar studies which include  $M_{\text{BH}}$ . Columns descriptions, (1) survey name, (2) detector (3) type of AGN analysed (4) total number of AGN in survey (5) Number of AGN with at least one good 10 ks light-curve segment and in brackets number used in our  $\sigma_{\text{NXS}}^2$  analysis with five or more segments. (6),(7) as (5) for 20 ks and 40 ks light-curve segments. (8) redshift range.

Segment duration [ks] (1)	Norm. $\pi$ (2)	Slope $\alpha$ (3)	Scatter $\sigma$ (4)	Correlation unweighted (5)	Correlation weighted (6)
10	0.0065 $\pm$ 0.0012	-0.47 $\pm$ 0.08	1.31 $\pm$ 0.15	-0.63	-0.66
20	0.0072 $\pm$ 0.0019	-0.45 $\pm$ 0.10	1.57 $\pm$ 0.22	-0.58	-0.69
20 <sup>CAIXA</sup>	0.0070 $\pm$ 0.0018	-0.60 $\pm$ 0.21	1.53 $\pm$ 0.21	-0.60	-0.60
40	0.0079 $\pm$ 0.0037	-0.45 $\pm$ 0.16	1.93 $\pm$ 0.43	-0.59	-0.56

**Table 3.** Correlations between hard-band  $L_X$  and  $\sigma_{\text{NXS}}^2$  of the form  $\log(\sigma_{\text{NXS}}^2) = \pi \log(L/L_{\text{piv}})^\alpha$  where there are five or more good light-curve segments for each of the segment durations length in column (1). (2) normalisation, (3) slope, (4)  $\sigma$  scatter, (5) Pearson’s product moment correlation coefficient, (6) as (5) weighted on  $\sigma_{\text{NXS}}^2$  error.  $L_{\text{piv}} = 2 \times 10^{43} \text{ erg s}^{-1}$ . <sup>CAIXA</sup> Results from (Bianchi et al. 2009a) survey with our fitting methodology.

Segment duration [ks] (1)	Normalisation $\pi$ (2)	Slope $\alpha$ (3)	Scatter $\sigma$ (4)	Correlation unweighted (5)	Correlation weighted (6)
10	0.0026 $\pm$ 0.001	-1.13 $\pm$ 0.20	1.09 $\pm$ 0.38	-0.91	-0.92
20	0.0036 $\pm$ 0.0013	-1.07 $\pm$ 0.18	1.01 $\pm$ 0.4	-0.93	-0.95
40	0.075 $\pm$ 0.054	-1.31 $\pm$ 0.5	1.53 $\pm$ 1.11	-0.91	-0.91

**Table 4.** Correlations between black hole mass from (Bentz & Katz 2015) and  $\sigma_{\text{NXS}}^2$  of the form  $\log(\sigma_{\text{NXS}}^2) = \pi \log(M/M_{\text{piv}})^\alpha$  where there are five or more good light curve segments for each of the segment durations length in column (1). (2) normalisation, (3) slope, (4)  $\sigma$  scatter, (5) Pearson’s product moment correlation coefficient, (6) as (5) weighted on  $\sigma_{\text{NXS}}^2$  error.  $M_{\text{piv}} = 2 \times 10^7 M_\odot$

$L_X$ method	Normalisation	Slope	Scatter	Correlation	Correlation
(1)	$\pi$ (2)	$\alpha$ (3)	$\sigma$ (4)	unweighted (5)	weighted (6)
Spectral fitting from full obs. duration	0.1155 $\pm$ 0.0303	1.34 $\pm$ 0.15	1.36 $\pm$ 0.20	0.87	0.94
From count-rate of eight passes of eROSITA duration	0.1076 $\pm$ 0.037	1.38 $\pm$ 0.19	1.25 $\pm$ 0.35	0.87	0.91

**Table 5.** Correlations between black hole mass from (Bentz & Katz 2015) and  $L_X$  of the form  $\log(L_X) = \pi \log(M/M_{\text{piv}})^\alpha$ . Method to determine  $L_X$  (1). (2) normalisation, (3) slope, (4)  $\sigma$  scatter, (5) Pearson's product moment correlation coefficient, (6) as (5) weighted on  $L_X$  error.  $M_{\text{piv}} = 2 \times 10^7 M_\odot$

XCS Source	z	$\log(L_X)$ erg s $^{-1}$
XMMXCSJ021557.6-045010.3	0.884	44.03 $\pm$ <sup>0.12</sup> <sub>0.02</sub>
XMMXCSJ021628.3-040146.8	0.830	44.46 $\pm$ <sup>0.14</sup> <sub>0.02</sub>
XMMXCSJ021659.7-053204.0	2.81	45.80 $\pm$ <sup>0.09</sup> <sub>0.01</sub>
XMMXCSJ021910.5-055114.0	0.558	44.22 $\pm$ <sup>0.09</sup> <sub>0.01</sub>
XMMXCSJ022024.9-061732.1	0.139	43.12 $\pm$ <sup>0.16</sup> <sub>0.02</sub>
XMMXCSJ022249.5-051453.7	0.314	44.08 $\pm$ <sup>0.09</sup> <sub>0.02</sub>
XMMXCSJ022258.8-045854.8	0.466	43.69 $\pm$ <sup>0.30</sup> <sub>0.04</sub>
XMMXCSJ022415.7-041418.4	1.653	44.47 $\pm$ <sup>0.10</sup> <sub>0.01</sub>
XMMXCSJ022452.1-040519.7	0.695	43.89 $\pm$ <sup>0.23</sup> <sub>0.03</sub>
XMMXCSJ022711.8-045037.4	0.961	44.49 $\pm$ <sup>0.06</sup> <sub>0.02</sub>
XMMXCSJ022716.1-044537.6	0.721	44.53 $\pm$ <sup>0.10</sup> <sub>0.02</sub>
XMMXCSJ022845.6-043350.7	1.865	45.50 $\pm$ <sup>0.07</sup> <sub>0.01</sub>
XMMXCSJ022851.4-051224.4	0.316	44.13 $\pm$ <sup>0.05</sup> <sub>0.03</sub>
XMMXCSJ033208.9-274732.1	0.544	43.91 $\pm$ <sup>0.03</sup> <sub>0.02</sub>
XMMXCSJ033211.5-273727.8	1.570	44.48 $\pm$ <sup>0.25</sup> <sub>0.00</sub>

**Table 6.** Estimated hard-band  $L_X$  from spectral fitting of AGN within OzDES reverberation mapping survey for AGN point sources not already in our Initial Sample as defined in Table 1.



XCS Name	AGN Name	Type	$z$	$\log(L_X)$ $\text{erg s}^{-1}$	$\Gamma$	$\sigma_{\text{NXS}}^2[10\text{ks}]$	N[10ks]	$\sigma_{\text{NXS}}^2[20\text{ks}]$	N[20ks]	$\sigma_{\text{NXS}}^2[40\text{ks}]$	N[40ks] , $M_\odot$	$\log(M_{\text{BH}})$
(1)	(2)	(3)	(4)	(5)	(6)	(7)	(8)	(9)	(10)	(11)	(12)	(13)
J000619.5+201210.3	MARK 335	1	0.026	$42.84 \pm 0.003$	1.52	$0.01 \pm 0.005$	34	$0.013 \pm 0.007$	11	$0.031 \pm 0.017$	5	$7.23 \pm 0.042$
J001030.9+105829.6	MARK 1501	1	0.089	$44.13 \pm 0.026$	1.2							$8.067 \pm 0.044$
J004153.3+402116.1	MARK 957	1	0.073	$42.84 \pm 0.031$	1.84	$0.015 \pm 0.006$	5					$8.067 \pm 0.165$
J005452.3+252538.1	2E 217	1.2	0.155	$44.58 \pm 0.007$	2.03							$8.462 \pm 0.083$
J010516.7-582615.8	ESO 113-G10	1.8	0.026	$42.68 \pm 0.003$	2.34	$0.01 \pm 0.005$	9	$0.019 \pm 0.01$	5			$8.462 \pm 0.094$
J012345.6-584822.5	F 9	1	0.046	$43.82 \pm 0.003$	2.25	$0 \pm 0.001$	12					$8.299 \pm 0.078$
J021433.4-004601.4	NGC 863	1	0.027	$42.89 \pm 0.014$	1.35							$7.57 \pm 0.119$
J023005.5-085953.4	MARK 1044	1	0.017	$42.81 \pm 0.012$	1.83	$0.026 \pm 0.008$	13	$0.032 \pm 0.012$	6			$7.57 \pm 0.062$
J023437.9-084715.2	NGC 985	1.5	0.043	$43.59 \pm 0.004$	1.47			$0.001 \pm 0.001$	5			$7.57 \pm 0.074$
J032240.5-371637.2	IXO 10	2	0.515	$43.85 \pm 0.035$	1.95	$0.011 \pm 0.064$	5	$0.012 \pm 0.035$	5			
J033301.7-275819.2	ECDF-S 441	1	1.842	$44.84 \pm 0.016$	2.25			$0.445 \pm 0.856$	6			
J033312.0-361947.9	MS 03313-3629	BL	0.308	$44.43 \pm 0.009$	1.92			$0 \pm 0.008$	29			
J033336.4-360826.1	NGC 1365	1.8	0.0060	$41.2 \pm 0.036$	0.07	$0.011 \pm 0.004$	41	$0.012 \pm 0.003$	25	$0.017 \pm 0.007$	12	
J033841.3-353132.8	CXOMP J03386-3531	1	0.36	$43.95 \pm 0.043$	2.17	$0.002 \pm 0.018$	12	$-0.093 \pm 0.134$	7			
J043311.0+052116.1	MARK 1506	1.5	0.033	$44.92 \pm 0.003$	1.64							$7.745 \pm 0.038$
J051045.4+162956.7	2E 1228	1.5	0.017	$43.2 \pm 0.003$	1.41							$6.876 \pm 0.04$
J051611.4-000859.5	AKN 120	1	0.033	$44.57 \pm 0.001$	1.66	$0 \pm 0$	17	$0 \pm 0$	13	$0 \pm 0$	8	$6.876 \pm 0.074$
J051621.1-103342.3	MCG -02.14.009	1	0.028	$43.27 \pm 0.003$	1.58	$0.001 \pm 0.002$	11	$0.007 \pm 0.006$	5			$8.068 \pm 0.424$
J053159.9-691951.4	1WGA J0531.9-6919	1	0.149	$43.03 \pm 0.05$	1.83	$0.004 \pm 0.02$	5					$8.068 \pm 0.048$
J055802.0-382002.9	H 0557-385	1.2	0.034	$42.85 \pm 0.017$	0.46	$0.028 \pm 0.011$	5	$0.011 \pm 0.011$	5			$8.068 \pm 0.063$
J055947.3-502652.2	PKS 0558-504	1	0.137	$45.57 \pm 0.002$	2.3	$0.006 \pm 0.002$	33	$0.012 \pm 0.004$	18	$0.024 \pm 0.013$	9	
J074232.7+494833.3	MARK 79	1.2	0.022	$42.92 \pm 0.006$	1.99	$0.001 \pm 0.001$	5				$7.612 \pm 0.107$	
J081058.6+760243.0	2E 1919	1	0.1	$44.17 \pm 0.006$	2.29						$7.612 \pm 0.136$	
J083538.8-040517.0	NGC 2617	1.8	0.014	$43 \pm 0.002$	1.42	$0 \pm 0$	5					$8.735 \pm 0.048$
J084742.5+344504.0	Ton 951	1	0.064	$42.98 \pm 0.016$	0.91							$8.735 \pm 0.05$
J091826.0+161822.6	MARK 704	1.2	0.029	$43.31 \pm 0.004$	2.11	$0.004 \pm 0.002$	6	$0.003 \pm 0.002$	5			$7.858 \pm 0.016$
J092512.7+521711.7	MARK 110	1	0.035	$43.87 \pm 0.004$	1.68							$7.292 \pm 0.11$
J094233.2+093836.3	MS 09398+0952	1	0.205	$43.12 \pm 0.038$	2.29	$0.044 \pm 0.04$	5					$7.292 \pm 0.097$
J095651.9+411519.7	2XMM J095652.4+411522	1	0.239	$44.69 \pm 0.009$	2.08							$8.333 \pm 0.062$
J095847.4+653353.9	S4 0954+65	BL	0.367	$44.89 \pm 0.006$	1.31	$0.001 \pm 0.007$	5					$8.333 \pm 0.11$
JJ100200.1-080945.0	IRAS 09595-0755	1	0.055	$43.3 \pm 0.011$	1.97	$0.003 \pm 0.002$	6					
J102348.6+040553.7	ACIS J10212+0421	1	0.099	$42.17 \pm 0.135$	3.85	$0.044 \pm 0.016$	14	$0.02 \pm 0.033$	9			
J103118.3+505333.9	1ES 1028+511	BL	0.361	$45.42 \pm 0.002$	2.32			$0 \pm 0.001$	8			
J103438.6+393825.8	KUG 1031+398	1	0.042	$42.12 \pm 0.011$	2.48	$0.011 \pm 0.005$	23	$0.01 \pm 0.005$	13	$0.012 \pm 0.005$	5	
J103935.5+533037.2	1AXG J103934+5330	1	0.229	$43.7 \pm 0.028$	1.74	$0.012 \pm 0.014$	7	$0.015 \pm 0.008$	5			
J105421.1+572544.1	RX J10543+5725	1	0.205	$44.03 \pm 0.014$	1.51	$0.003 \pm 0.006$	12					
J110647.4+723407.0	NGC 3516	1.5	0.0090	$42.45 \pm 0.003$	0.85	$0.004 \pm 0.002$	24	$0.006 \pm 0.003$	12	$0.008 \pm 0.005$	6	$7.395 \pm 0.06$
J112916.6-042407.6	MARK 1298	1	0.06	$42.59 \pm 0.022$		$0.041 \pm 0.036$	5					$7.395 \pm 0.06$
J114008.7+030711.1	SDSS J11401+0307	1	0.081	$42.56 \pm 0.014$	2.41	$0.038 \pm 0.01$	10	$0.044 \pm 0.023$	5			
J115851.2+435046.3	SDSS J11588+4350	1	0.287	$44.11 \pm 0.391$	5.07	$0.043 \pm 0.036$	5					
J115941.0-195923.3	CTS J08.06	1	0.456	$45.31 \pm 0.002$	1.65	$0.002 \pm 0$	5					
J120114.3-034039.6	MARK 1310	1	0.019	$41.85 \pm 0.015$	1.73							$6.212 \pm 0.06$
J120256.9-205602.9	POX 52	1.8	0.022	$42.06 \pm 0.015$	0.64	$0.073 \pm 0.016$	7					$6.212 \pm 0.06$
J120309.5+443153.0	NGC 4051	1	0.0020	$41.16 \pm 0.003$	1.53	$0.061 \pm 0.012$	39	$0.068 \pm 0.013$	23	$0.08 \pm 0.019$	7	$6.13 \pm 0.11$
J121417.6+140313.9	PG 1211+143	1	0.082	$43.72 \pm 0.003$	1.78	$0.005 \pm 0.001$	31	$0.009 \pm 0.003$	16	$0.01 \pm 0.003$	8	$6.13 \pm 0.11$
J121651.9+375436.1	MS 12143+3811	1	0.063	$42.53 \pm 0.026$	2.13	$0.021 \pm 0.006$	9					
J121826.5+294847.1	MARK 766	1	0.013	$42.62 \pm 0.003$	1.77	$0.021 \pm 0.009$	46	$0.023 \pm 0.006$	27	$0.056 \pm 0.034$	13	$6.822 \pm 0.05$

AGN to AGN black hole mass correlations

XCS Name	AGN Name	Type	$z$	$\log(L_X)$ $\text{erg s}^{-1}$	$\Gamma$	$\sigma_{\text{NXS}}^2[10\text{ks}]$	N[10ks]	$\sigma_{\text{NXS}}^2[20\text{ks}]$	N[20ks]	$\sigma_{\text{NXS}}^2[40\text{ks}]$	N[40ks] , $M_\odot$	$\log(M_{\text{BH}})$
(1)	(2)	(3)	(4)	(5)	(6)	(7)	(8)	(9)	(10)	(11)	(12)	(13)
J122206.7+752616.3	XMM J12221+7526	2	0.238	$43.81 \pm 0.02$	1.56	$0.002 \pm 0.017$	5					
J122324.2+024044.9	MARK 50	1.2	0.023	$43.01 \pm 0.017$	1.94							$7.422 \pm 0.006$
J122548.8+333249.0	NGC 4395	1.8	0.0010	$40.84 \pm 0.01$	0.86	$0.195 \pm 0.066$	11	$0.246 \pm 0.032$	5			$5.449 \pm 0.017$
J122906.6+020309.0	3C 273.0	1	0.158	$46 \pm 0.001$	1.57	$0 \pm 0$	14	$0 \pm 0$	5			$8.839 \pm 0.001$
J123147.1+123836.7	SDSS J12317+1238	1	0.292	$43.51 \pm 0.092$	2.41	$0.001 \pm 0.006$	5					
J123203.7+200928.1	MARK 771	1	0.064	$43.45 \pm 0.016$	2.2							$7.758 \pm 0.019$
J123800.8+621337.1	Q 1235+6230	1	0.44	$43.47 \pm 0.096$	3.99	$0.015 \pm 0.081$	11					
J123939.4+052043.3	NGC 4593	1	0.0090	$42.81 \pm 0.016$	2.35							$6.882 \pm 0.084$
J124210.5+331701.9	WAS 61	1	0.045	$43.37 \pm 0.003$	2.1	$0.006 \pm 0.002$	7					
J124635.1+022210.2	PG 1244+026	1	0.048	$43.14 \pm 0.005$	2.42	$0.017 \pm 0.005$	12	$0.027 \pm 0.009$	6			
J124938.4+050925.5	SDSS J12496+0509	1	0.991	$44.92 \pm 0.025$	2.07	$0.023 \pm 0.061$	6					
J124955.3+051629.0	SDSS J12499+0516	1	0.212	$43.05 \pm 0.041$	1.28	$0.02 \pm 0.026$	5					
J125611.1-054720.7	3C 279	Q	0.538	$45.92 \pm 0.002$	1.58			$0 \pm 0.001$	6			
J130022.1+282402.8	X COM	1.5	0.092	$43.57 \pm 0.005$	2.33	$0.003 \pm 0.001$	8	$0.002 \pm 0.002$	10	$0.003 \pm 0.002$	7	
J130028.7+283008.7	5C 4.105	1.2	0.645	$44.97 \pm 0.008$	1.71	$0.006 \pm 0.006$	19					
J132519.2-382455.2	IRAS 13224-3809	1	0.065	$42.66 \pm 0.009$	2.53	$0.117 \pm 0.03$	42	$0.157 \pm 0.03$	25	$0.217 \pm 0.049$	13	
J133553.7-341745.5	MCG -06.30.015	1.5	0.0080	$42.55 \pm 0.004$	1.6	$0.022 \pm 0.008$	27	$0.032 \pm 0.015$	16	$0.048 \pm 0.014$	8	
J133718.9+242303.2	IRAS 13349+2438	1	0.107	$44 \pm 0.008$	1.69	$0.005 \pm 0.003$	5	$0.008 \pm 0.003$	6			
J134208.4+353916.1	NGC 5273	1.9	0.0030	$41.13 \pm 0.008$	1.21							$6.66 \pm 0.125$
J135303.7+691828.9	MARK 279	1	0.031	$43.51 \pm 0.003$	1.83							$7.435 \pm 0.099$
J141759.5+250812.2	NGC 5548	1.5	0.017	$43.4 \pm 0.003$	1.8	$0.002 \pm 0.001$	41	$0.001 \pm 0.001$	23	$0.002 \pm 0.001$	13	$7.718 \pm 0.016$
J141922.4-263841.1	ESO 511-G030	1	0.022	$44.03 \pm 0.002$	2.05	$0 \pm 0$	10	$0.001 \pm 0$	5			
J142832.6+424021.4	H 1426+428	1	0.129	$44.91 \pm 0.005$	1.94	$0 \pm 0$	17	$0 \pm 0$	11	$0 \pm 0$	6	
J150401.1+102616.4	MARK 841	1.5	0.036	$43.45 \pm 0.004$	1.27	$0.002 \pm 0.001$	5					
J153552.2+575411.7	MARK 290	1.5	0.03	$43.23 \pm 0.006$	1.47	$0.004 \pm 0.001$	6					$7.277 \pm 0.061$
J155543.0+111125.4	PG 1553+11	BL	0.36	$45.42 \pm 0.001$	2.28	$0 \pm 0$	22	$0.001 \pm 0$	17	$0 \pm 0$	12	
J163323.7+471857.6	RXS J16333+4718	1	0.116	$43.66 \pm 0.017$	1.64	$0.023 \pm 0.006$	6					
J164823.2+350324.4	SDSS J16483+3503	1	0.178	$43.5 \pm 0.044$	1.45	$0.016 \pm 0.022$	6					
J165640.6+275257.7	SDSS J16566+2752	1	0.195	$43.72 \pm 0.058$	1.14	$0.007 \pm 0.013$	5					
J172819.6-141555.7	PDS 456	Q	0.184	$44.45 \pm 0.021$	2.26	$0.002 \pm 0.001$	37	$0.004 \pm 0.001$	32	$0.007 \pm 0.003$	15	
J190525.8+422739.8	Z 229-15	1	0.027	$42.8 \pm 0.006$	1.62							$6.913 \pm 0.075$
J194240.5-101924.5	NGC 6814	1.5	0.0050	$42.09 \pm 0.003$	1.49							$7.038 \pm 0.056$
J204409.7-104325.8	MARK 509	1.5	0.035	$44.03 \pm 0.002$	2.13	$0 \pm 0$	30	$0 \pm 0$	28	$0.001 \pm 0.001$	11	$8.049 \pm 0.035$
J213227.8+100819.6	MARK 1513	1.5	0.061	$43.47 \pm 0.02$	1.69							$7.433 \pm 0.055$
J213631.6+003153.1	MS 21340+0018	Q	0.805	$44.63 \pm 0.023$	1.73			$0.02 \pm 0.075$	6			$7.433 \pm 0.063$
J215852.0-301332.4	PKS 2155-304	BL	0.116	$44.75 \pm 0.003$	2.65	$0.001 \pm 0$	40	$0.001 \pm 0$	22	$0.003 \pm 0.001$	7	
J220916.1-470959.2	NGC 7213	1	0.0060	$41.96 \pm 0.003$	1.93			$-0.001 \pm 0$	6			
J221918.4+120754.4	II Zw 177	1	0.082	$42.94 \pm 0.009$	2.41	$0.021 \pm 0.016$	12	$0.034 \pm 0.023$	6			
J224239.3+294331.9	AKN 564	2	0.025	$43.89 \pm 0.002$	2.55	$0.025 \pm 0.008$	29	$0.036 \pm 0.011$	13	$0.044 \pm 0.011$	6	
J225405.9-173459.3	MR 2251-178	1.5	0.064	$44.3 \pm 0.002$	1.39	$0 \pm 0$	9	$0 \pm 0$	7	$0 \pm 0$	6	
J225739.1-365605.1	MS 22549-3712	1	0.039	$42.9 \pm 0.004$	2.33	$0.006 \pm 0.003$	7					
J230315.6+085223.9	NGC 7469	1.5	0.017	$43.25 \pm 0.002$	1.95	$0.001 \pm 0$	7	$0.002 \pm 0$	5			$6.956 \pm 0.048$

Table 7: Parameters derived or from literature for combined S10, S20 and S40 samples (1) XCS point source name, (2) AGN name if given from literature (3) AGN Type if given from VC13 or SIMBAD, 1, 2 and intermediate, Q-Quasar, BL-BL Lac (4) redshift (5)  $\log$  hard-band luminosity  $\text{erg s}^{-1}$  (6) hard-band photon spectral index (7) 10 ks light-curve  $\sigma_{\text{NXS}}^2$  value (8) number of AGN with five or more good 10 ks light-curve segments, (9) - (12) as (7) and (8) for 20 ks and 40 ks light-curve segments. (13) Black hole mass  $M_\odot$  from (Bentz & Katz 2015)

This paper has been typeset from a  $\text{\TeX}/\text{\LaTeX}$  file prepared by the author.